

(4)

DTIC FILE COPY

CHARACTERIZATION AND MODELING OF THORACO-ABDOMINAL RESPONSE TO BLAST WAVES

AD-A189 668

Volume 2. Blast Load Definition on a Torso Model

Annual/Final Report

May 1985

DTIC
ELECTE
FEB 1 5 1988
S D

James H.-Y. Yu
Ralph E. Ferguson
Edward J. Vassel
David A. Sargis

James H. Stuhmiller, Principal Investigator

JAYCOR
11011 Torreyana Road
San Diego, California 92121

Contract No. DAMD17-82-C-2062

Supported by

U. S. Army Medical Research and Development Command
Fort Detrick, Frederick, Maryland 21701

Approved for public release; distribution unlimited

88 2 12 053

The findings in this report are not to be construed as an official Department of the Army position unless so designated by other authorized documents.

Accession For	
NTIS CRA&I	<input checked="checked" type="checkbox"/>
DTIC TAB	<input type="checkbox"/>
Unannounced	<input type="checkbox"/>
Justification	
By	
Distribution /	
Availability Codes	
Dist	Availability / or special
A-1	



REPORT DOCUMENTATION PAGE

Form Approved
CMB No. 0704-0188

1a. REPORT SECURITY CLASSIFICATION UNCLASSIFIED			1b. RESTRICTIVE MARKINGS		
2a. SECURITY CLASSIFICATION AUTHORITY			3. DISTRIBUTION/AVAILABILITY OF REPORT Approved for public release; distribution unlimited		
2b. DECLASSIFICATION/DOWNGRADING SCHEDULE			5. MONITORING ORGANIZATION REPORT NUMBER(S)		
4. PERFORMING ORGANIZATION REPORT NUMBER(S)			7a. NAME OF MONITORING ORGANIZATION		
6a. NAME OF PERFORMING ORGANIZATION JAYCOR		6b. OFFICE SYMBOL (if applicable)		7b. ADDRESS (City, State, and ZIP Code)	
6c. ADDRESS (City, State, and ZIP Code) 11011 Torreyana Road San Diego, California 92121		8a. NAME OF FUNDING/SPONSORING ORGANIZATION U.S. Army Medical Research & Development Command		8b. OFFICE SYMBOL (if applicable)	
8c. ADDRESS (City, State, and ZIP Code) Fort Detrick Frederick, Maryland 21701-5012		9. PROCUREMENT INSTRUMENT IDENTIFICATION NUMBER DAMD17-82-C-2062			
10. SOURCE OF FUNDING NUMBERS		PROGRAM ELEMENT NO.		PROJECT NO. 3M1	TASK NO. CG
		61102A		61102BS10	087
11. TITLE (Include Security Classification) (U) Characterization and Modeling of Thoraco-Abdominal Response to Blast Waves Volume 2. Blast Load Definition on a Torso Model					
12. PERSONAL AUTHOR(S) James H.-Y. Yu, Ralph E. Ferguson, Edward Vassel, David A. Sargis, and James H. Stuhmiller					
13a. TYPE OF REPORT Annual/Final		13b. TIME COVERED FROM 2/15/82 TO 5/31/85		14. DATE OF REPORT (Year, Month, Day) 1985 May	
15. PAGE COUNT 60					
16. SUPPLEMENTARY NOTATION Annual covers time period of 15 February 1984 - 31 May 1985. Annual/Final published in 8 volumes					
17. COSATI CODES			18. SUBJECT TERMS (Continue on reverse if necessary and identify by block number)		
FIELD	GROUP	SUB-GROUP			
06	21				
06	17				
19. ABSTRACT (Continue on reverse if necessary and identify by block number)					
20. DISTRIBUTION/AVAILABILITY OF ABSTRACT <input type="checkbox"/> UNCLASSIFIED/UNLIMITED <input checked="" type="checkbox"/> SAME AS RPT. <input type="checkbox"/> DTIC USERS					
22a. NAME OF RESPONSIBLE INDIVIDUAL Mary Frances Bostian			21. ABSTRACT SECURITY CLASSIFICATION Unclassified		22c. OFFICE SYMBOL SGRD-RMI-S
			22b. TELEPHONE (Include Area Code) 301-663-7325		

FOREWORD

This Annual/Final Report has eight volumes. The titles are as follows:

1. Project Summary
2. Blast Load Definition on a Torso Model
3. Lung Dynamics and Mechanical Properties Determination
4. Biomechanical Model of Thorax Response to Blast Loading
5. Experimental Investigation of Lung Injury Mechanism
6. Biomechanical Model of Lung Injury Mechanisms
7. Gastrointestinal Response to Blast
8. Effect of Clothing on Thoracic Response

CONTENTS

	<u>Page</u>
1. INTRODUCTION	1
2. DESIGN AND FABRICATION OF TORSO MODEL	3
3. FIELD TESTS	7
4. COMPARISON WITH EITACC CALCULATIONS	23
4.1 Description of the EITACC Code	23
4.2 Propagation of Blast Waves	24
4.3 Loading for a Nominal 3 psi Wave	28
4.4 Relation of Load Impulse to Free-Field Impulse	43
5. EFFECT OF SURFACE MATERIAL	49
6. SUMMARY AND CONCLUSIONS	55

ILLUSTRATIONS

	<u>Page</u>
2-1a. Engineering Drawing of the Load Definition Test Model	5
2-1b. Load Definition Test Model	6
3-1. Dynamic Calibration Test Setup	9
3-2. Model Geometry, Probe Locations and Blast Overpressure Incidence Angle	11
3-3. Load Definition Field Test Arrangement (model covered with moleskin)	12
3-4. Sample Output of Pressure Traces	14
3-5. Pressure Coefficient Around the Torso Model	16
3-6. Free Field Peak Pressure vs. A-duration	20
3-7. Comparison of Digitized Signal with Probe Output	21
4-1. 5.61 psi Pressure Wave Propagation as a Function of Time	25
4-2. 9.62 psi Pressure Wave Propagation as a Function of Time	26
4-3. 26.92 psi Pressure Wave Propagation as a Function of Time	27
4-4. Computational Mesh Plots for 9-90° Calculations	29
4-5. Vector Plots at 0°, 3.0 psi	30
4-6. Pressure Contours at 0°, 3.0 psi	30
4-7. Vector Plots at 30°, 3.39 psi	31
4-8. Pressure Contours at 30°, 3.39 psi	31
4-9. Vector Plots at 60°, 3.0 psi	32
4-10. Pressure Contours at 60°, 3.0 psi	32
4-11. Vector Plots at 90°, 3.38 psi	33
4-12. Pressure Contours at 90°, 3.38 psi	33
4-13. Comparison of Calculated and Measured Pressure Signals for Free Field and Probes, 3 psi wave, $\theta = 0^\circ$	34
4-14. Comparison of Calculated and Measured Pressure Signals for Free Field and Probes, 3.39 psi wave, $\theta = 30^\circ$	35
4-15. Comparison of Calculated and Measured Pressure Signals for Free Field and Probes, 3.0 psi wave, $\theta = 60^\circ$	36
4-16. Comparison of Calculated and Measured Pressure Signals for Free Field and Probes, 3.38 psi wave, $\theta = 90^\circ$	37
4-17. Comparison of Calculated and Measured Pressure Signals for Free Field and Probes, 3.61 psi wave, $\theta = 120^\circ$	38

4-18.	Comparison of Calculated and Measured Pressure Signals for Free Field and Probes, 3.69 psi wave, $\theta = 150^\circ$	39
4-19.	Comparison of Calculated and Measured Pressure Signals for Free Field and Probes, 3.04 psi wave, $\theta = 180^\circ$	40
4-20.	Comparison of Calculated and Measured Peak Pressures	41
4-21.	Comparison of Calculated and Measured Impulses	44
4-22.	Comparison of Calculated Normalized Impulsive Loadings for Nominal 3 psi Tests	46
4-23.	Comparison of Measured Normalized Impulsive Loadings for Nominal 3 psi Tests	47
4-24.	Comparison of Higher Pressure Normalized Impulse Loadings for $\theta = 0^\circ$	48
5-1.	Effect of Compliant Surface on Pressure Signals at $\theta = 0^\circ$	50
5-2.	Effect of Compliant Surface on Pressure Signals at $\theta = 90^\circ$	51
5-3.	Effect of Compliant Surface on Pressure Distribution Around a Torso Model at $\theta = 0^\circ$	52
5-4.	Effect of Compliant Surface on Pressure Distribution Around a Torso Model at $\theta = 90^\circ$	53

TABLES

	<u>Page</u>
3-1. Block Ranging Shots for 16-lb TNT Charge	8
3-2. Pulse Calibration vs. Dynamic Calibration	10
3-3. Summary of Torso Model Tests	15

1. INTRODUCTION

→ The first step in developing the methodology for connecting the blast environment to bodily injury is to determine the distribution of mechanical loading on a test subject exposed to blast loading. The loading will be used to drive a structural analysis calculation that will predict local, internal stresses that can be correlated with damage. This report describes the use of a computer code to connect the gas dynamics of a blast field to the pressure distribution on the body and the validation of those calculations by data taken in the field.

To make the validation process as pertinent as possible to the final application without being overly complex, a two-dimensional cross-sectional geometry was selected. A test fixture with the desired shape was constructed and instrumented. The data was reduced and compared with calculations made with JAYCOR's EITACC code.

Extensive validation was carried out at occupational exposure levels and the agreement was quite good. A correlation was developed for extending incident load impulse to higher level waves. ←

2. DESIGN AND FABRICATION OF TORSO MODEL

In order to validate the EITACC code for the prediction of loading on animal and human torsos, a model target was designed, fabricated, and two copies delivered to Lovelace for field tests.

This model was designed based on the following considerations.

- a. Realistic model dimensions.
- b. Minimal expenditures in material and labor.
- c. Easily instrumented and easily adjusted in orientation.
- d. Sufficient material strength to withstand blast loading.

Based on these considerations, the measurements of an "average" soldier were used for the model. A large diameter aluminum tube cut into two halves and welded together with two flat pieces in between was used to simulate the oblong-shaped chest. The torso model was welded to a base plate which can be later bolted in place with a guiding ring around it. The two arms, made of aluminum tubes, were mounted in place by sliding over two circular discs that were bolted to the base plate.

An aluminum cover plate, cut to match the outlines of the arms and the torso, was used to fix the relative locations of the pieces. The minimal overhang of the cover plate was designed to cut down the effect of possible pressure wave reflection. A 2" diameter opening at the center of the plate was provided for feeding pressure transducer cables.

To reduce the ground boundary layer and model end effects on the measured signal, the model was made 4 ft high and with the pressure transducers mounted at the midsection. Cross-talk among the transducers was prevented by threading each transducer into a delrin bushing before threading into the torso wall. The bushings were filled flush with the torso surface to prevent possible aerodynamic disturbances resulting from mounting port irregularities.

To facilitate the adjustment of model orientation (at 30° increments), twelve 5/8" dia. holes 30° apart were drilled in the base plate. For different model orientations the model will simply be rotated to the proper direction, aligned with a guiding hole on the mounting pad, and retightened.

The effect of clothing on the measured signal will be tested by covering the torso (and the transducers) with a moleskin jacket. This moleskin jacket is made of flannel material with 1/8" thick foam padding.

Figure 2-1a presents the engineering drawings of the model. Figure 2-1b shows pictures of the final product.

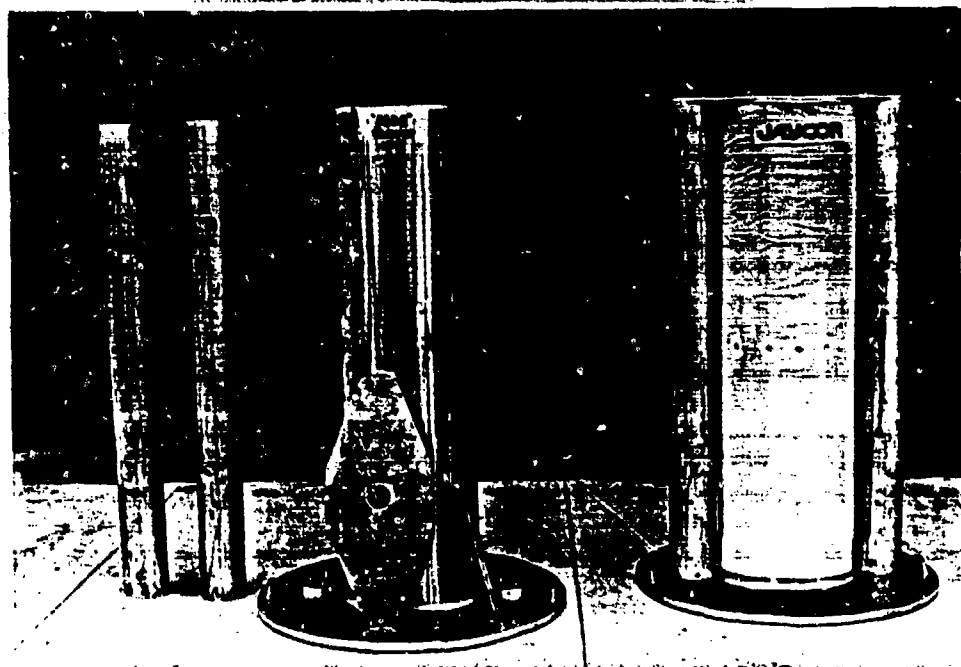
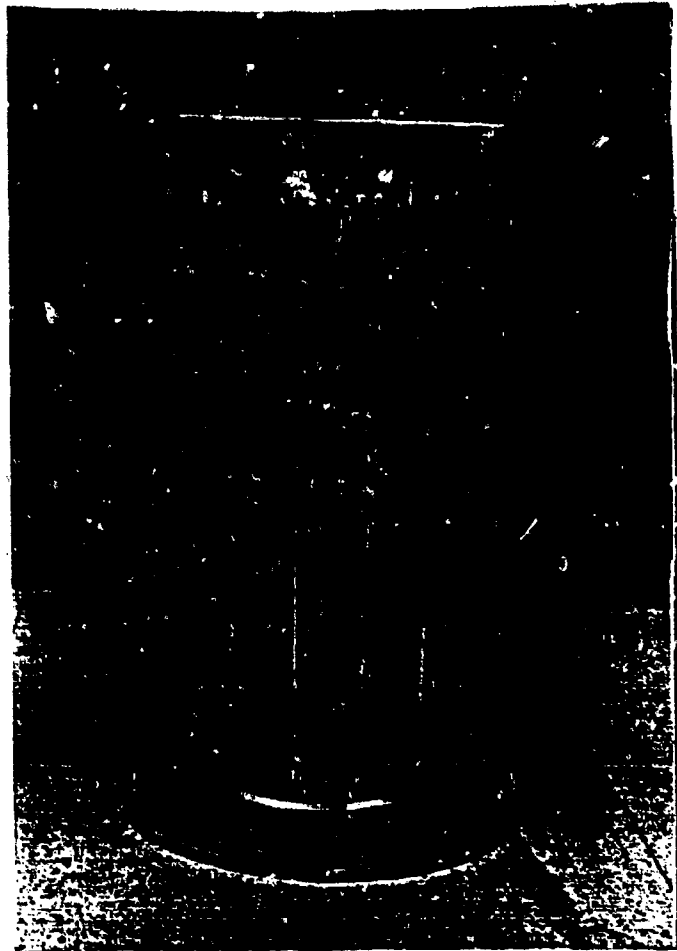


Figure 2-1b. Load definition test model

3. FIELD TESTS

The data required for the validation of the EITACC code was obtained from field tests conducted on July 13 through 15, 1982 at the test site of the Lovelace Inhalation Toxicology Research Institute (ITRI) in Albuquerque, New Mexico.

The tests used blast waves with nominal peak pressures of 3, 5, 10 and 25 psi. For each pressure level, model orientations ranging from 0° to 180° at 30° increments were tested. A 16 lb charge TNT was used for all tests. The desired pressure levels were obtained by varying the blast ranges.

The height of burst (HOB) was adjusted for each pressure level so that a shock stem higher than the torso model at the test range would be achieved. Within a shock stem, a uniform pressure front will be maintained. Table 3-1 summarizes the ranging shot test results.

PCB piezoelectric pressure transducers, model ST-2, were used for the pressure measurement on the model. These transducers were calibrated by two independent approaches: static calibration and dynamic calibration. A static calibration was carried out by mounting each transducer in a test chamber where a pressure pulse was delivered by the sudden opening of a solenoid valve that connected to a pressure chamber with a known pressure (10 psi in this case). The sensitivity of the probe was then determined by the probe's output. A dynamic calibration was achieved by the detonation of a 1 lb pentolite sphere. In this case, all the probes were mounted on a plate in a side-on position. At a 12.5 ft blast range, the pentolite charge will give a precise 10 psi overpressure and the corresponding output voltages were again used to determine the calibration factors for each probe. The arrangement of the dynamic calibration test setup is shown in Figure 3-1.

The calibration factors provided by ITRI, both before and after the load definition tests, are summarized in Table 3-2. Since the original probe nos. 4 and 5 failed to function properly at the beginning of the tests, they were

Table 3-1. Block Ranging Shots for 16-lb TNT Charge

Shot No.	Burst Height (ft)	Mach Stem Height (ft)	Horizontal Range (ft)	Slant Range (ft)	Peak Pressure (psi)			Duration (ms)		
					(G-8)	(G-7)	(mean)	(G-8)	(G-7)	(mean)
1	7.7	> 13	56.2	56.5	3.3	2.8	3.0	8.4	8.3	8.4
2	7.7	> 12	41.1	41.5	5.4	4.6	5.0	7.9	7.8	7.8
3	7.7	5.8	28.5	29.1	10.1	8.3	6.5	6.5	6.3	6.4
4	4.1	5.4	15.9	16.9	32.7	24.4	28.6	3.5	3.5	3.5

replaced by two different probes. Their pre-shot calibration factors were thus excluded from the table.

Though the static calibrations seem to have good repeatability (except probe no. 6 which has a 25% increase in its calibration factor) there are relatively large spreads for the readings between the static and the dynamic tests and among the outputs of each dynamic calibration set. The 14% spread in pre-shot calibration and 11% for the post-shot probably will be reflected in the reduced data.

Since the static calibrations seem to have less variation, those calibration factors were used for subsequent data reduction. In addition, since the post-shot calibration factor for probe no. 6 seems to be too high compared with the rest of the probes and with the pre-shot value, it was discarded. Instead, the average value of the pre-shot calibrations was used. (Such correction was found to make the data blend more smoothly with that of the rest of the probes.)

The locations of the probes on the model and the blast overpressure with respect to various model orientations are shown in Figure 3-2. A reference probe with a side-on sensing surface, located at the same range and probe height as the model probes, was used to measure the free field signal. An additional probe at a closer range was used as a trigger probe for the oscilloscope. The general setup of the blast tests is shown in Figure 3-3.

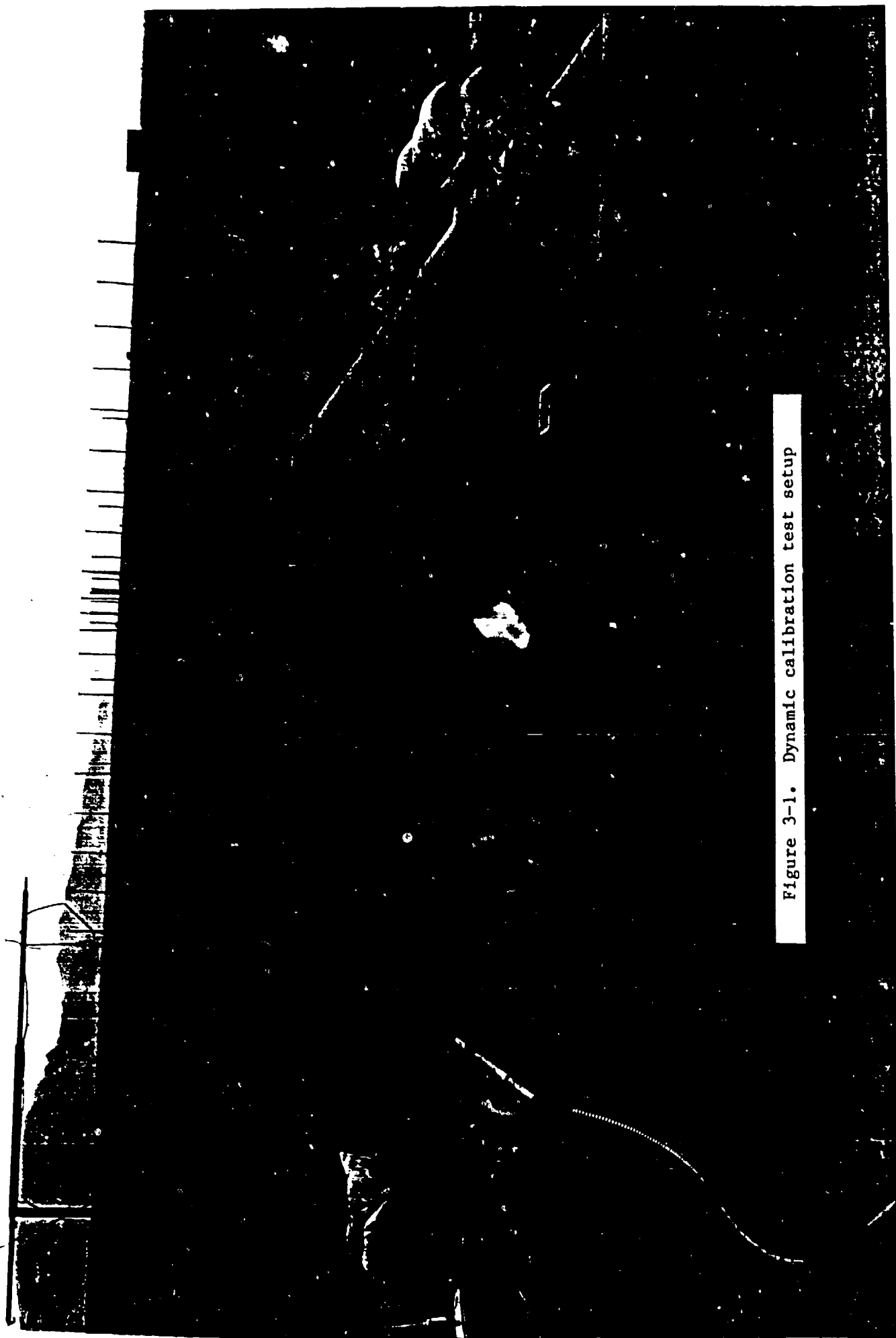


Figure 3-1. Dynamic calibration test setup

Table 3-2. Pulse Calibration vs Dynamic Calibration

a. Pre-Shot									
Gauge No.	S/N	Pulse Calibration			Dynamic Calibration				
		Amplifier Gain Factor	Calibrator Pressure (psi)	Deflection (div)	mv/psi × 2	Amplifier Gain Factor	Deflection (div)	Peak Pressure (psi)	
1	ST-2-55	2	10	2.38	4.202	23.8	2	2.32	9.7
2	ST-2-5103	2	10	2.48	4.032	24.8	2	2.30	9.3
3	ST-2-1277	2	10	2.39	4.184	23.9	2	2.23	9.3
4	ST-2-29	2	10	2.63	3.802	26.3	2	—	—
5	ST-2-112	2	10	2.76	3.623	27.6	2	—	—
6	ST-2-1274	2	10	2.56	3.906	25.6	2	2.20	8.6
7	ST-2-1275	2	10	2.55	3.922	25.5	2	2.32	9.1
8	ST-2-2050	2	10	2.60	3.846	26.0	2	2.41	9.3

b. Post-Shot									
1	ST-2-55	2	10	2.34	4.274	23.4	2	2.29	9.8
2	ST-2-5103	2	10	2.49	4.016	24.9	2	2.31	9.3
3	ST-2-1277	2	10	2.40	4.167	24.0	2	2.15	9.0
4	ST-2-29	2	10	2.69	3.717	26.9	2	2.64	9.8
5	ST-2-112	2	10	2.70	3.704	27.0	2	2.40	8.9
6	ST-2-1274	2	10	2.01	4.975	20.1	2	2.06	10.2
7	ST-2-1275	2	10	2.55	3.922	25.5	2	2.32	9.1
8	ST-2-2050	2	10	2.63	3.802	26.3	2	2.71	10.3

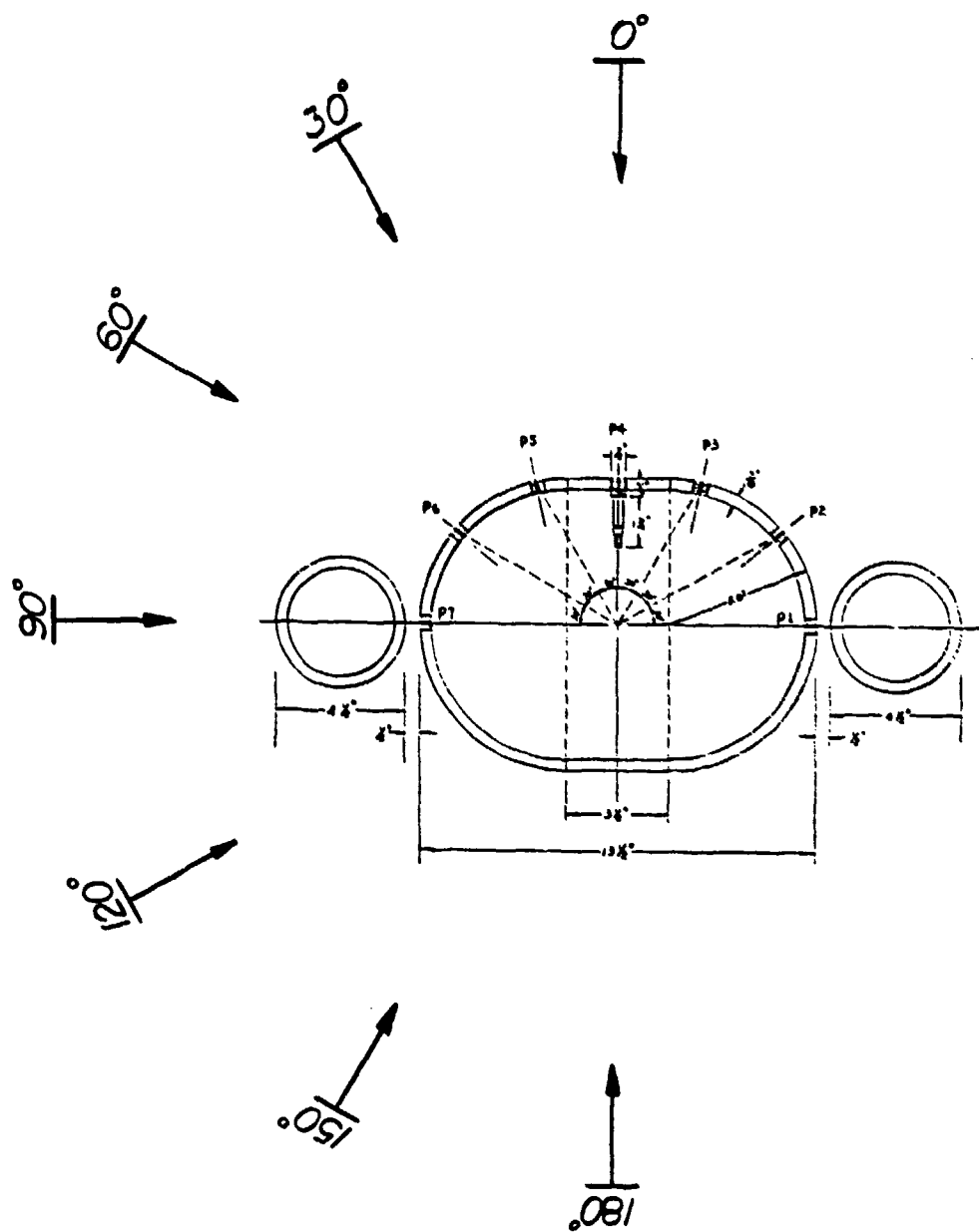


Figure 3-2. Model geometry, probe locations and blast overpressure incidence angle

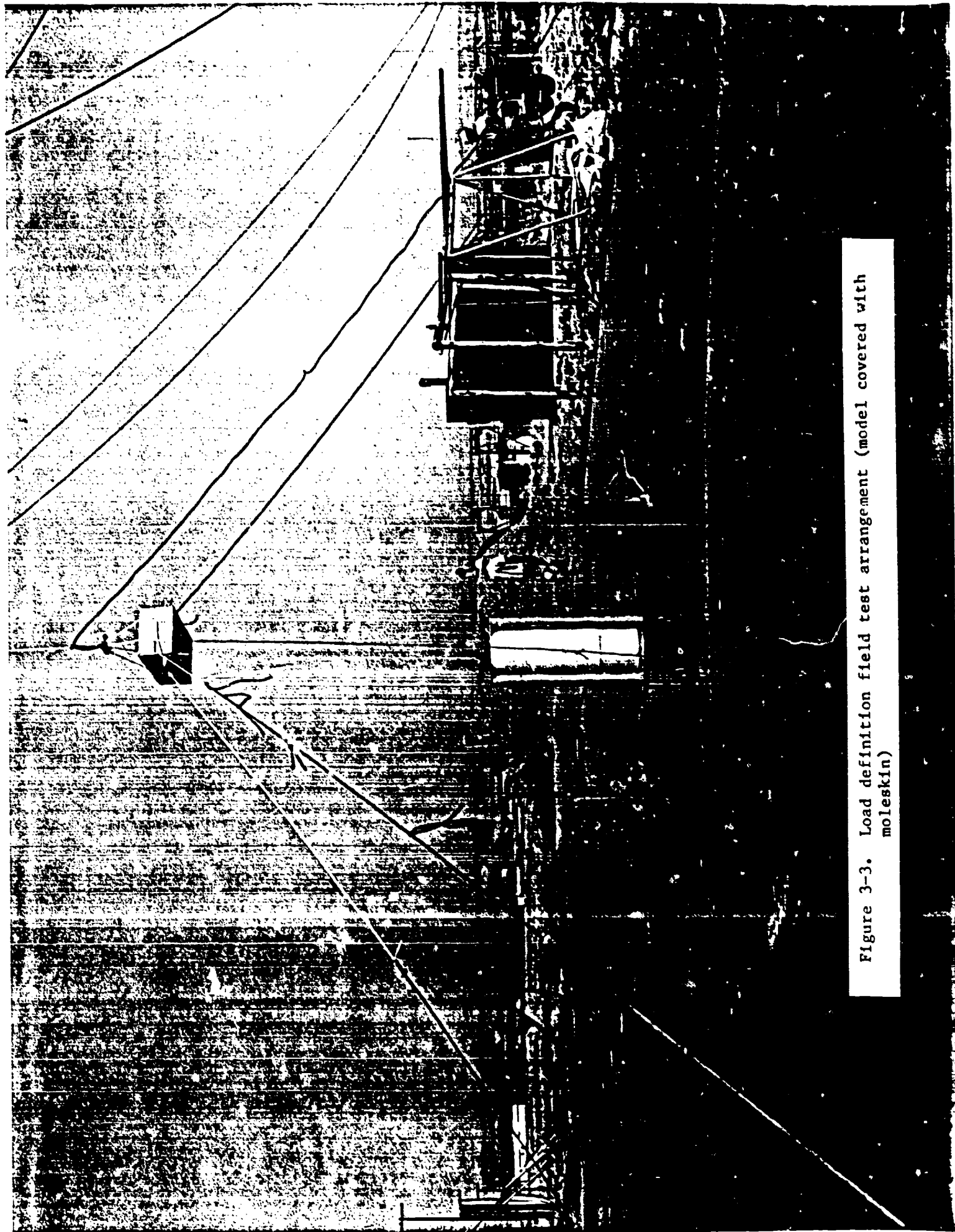


Figure 3-3. Load definition field test arrangement (model covered with moleskin)

For each test, the outputs from the seven model probes and the one reference probe (#8) were recorded by an analog tape recorder. Hard copies were then obtained from a strip chart recorder by playing back the tape at a reduced speed. A retrace of a sample hard copy is shown in Figure 3-4.

The complete data set including all orientations at all pressure levels was reduced by using the calibration factors provided by ITRI. The peak pressures are summarized in Table 3-3. These values are further non-dimensionalized by the free field reference pressure to show the extent of the "doubling effect," and are plotted in Figures 3-5a to 3-5d. Except for some scattered data points, the trend seems to be quite clear for each orientation. Furthermore, there seems little difference in the multiplying factors for each orientation between 3 and 5 psi cases and increased multiplying factors for higher pressures.

The free field pressures and their corresponding A-durations are also shown in Table 3-3. Though the tests were carried out with the same charge, there were significant variations in the magnitude for each pressure level. The results are summarized and replotted in Figure 3-6 to show the pressure-duration relationship.

In order to compare the data with the computer output, the signals were digitized directly off the hard copy by using JAYCOR's Tektronix digitizing system. This information was then fed into JAYCOR's Univac computer system for subsequent data analysis. The necessary computer programs were then written to calculate the impulses and to replot the results at the same scale as the computer output for comparison. Samples from the Tektronix digitizer, from the computer driven plotter, and the original hard copy are shown in Figure 3-7. As shown, the manual digitizing process was able to preserve the essential features of the original signal.

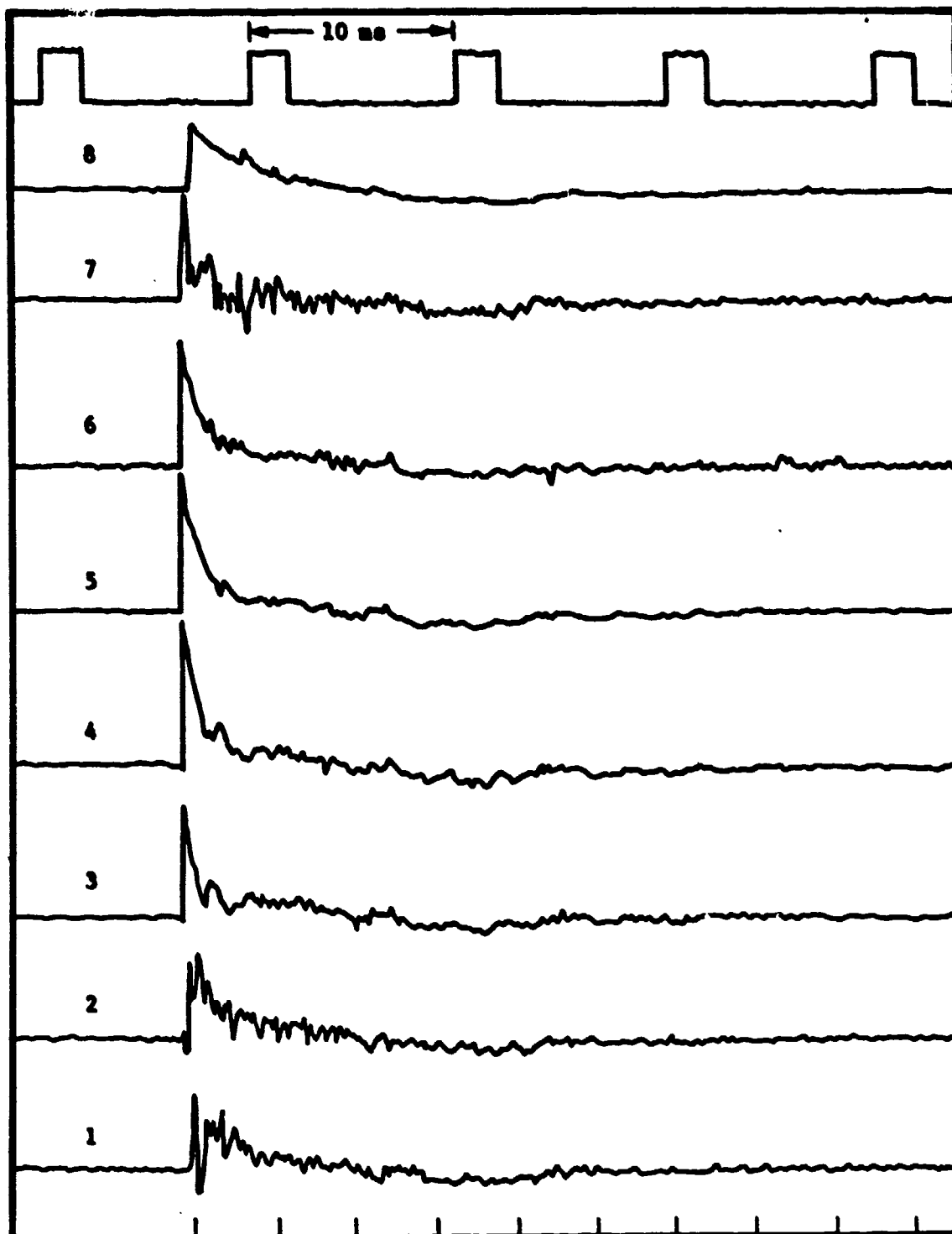
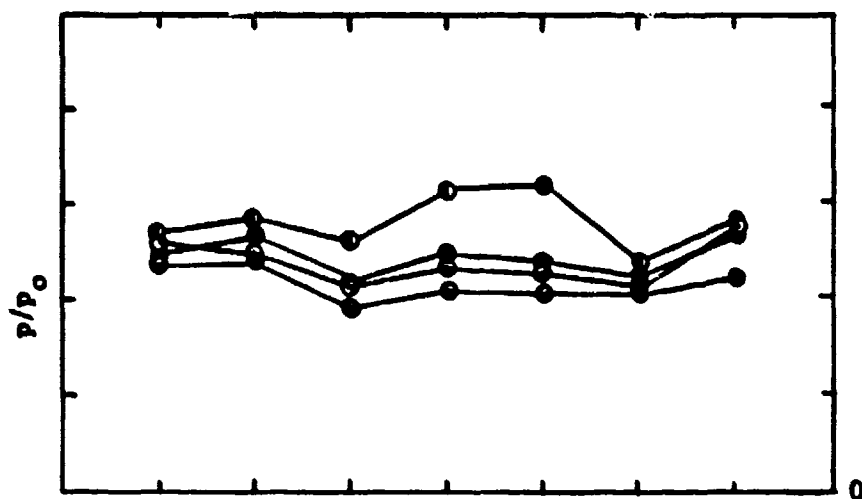


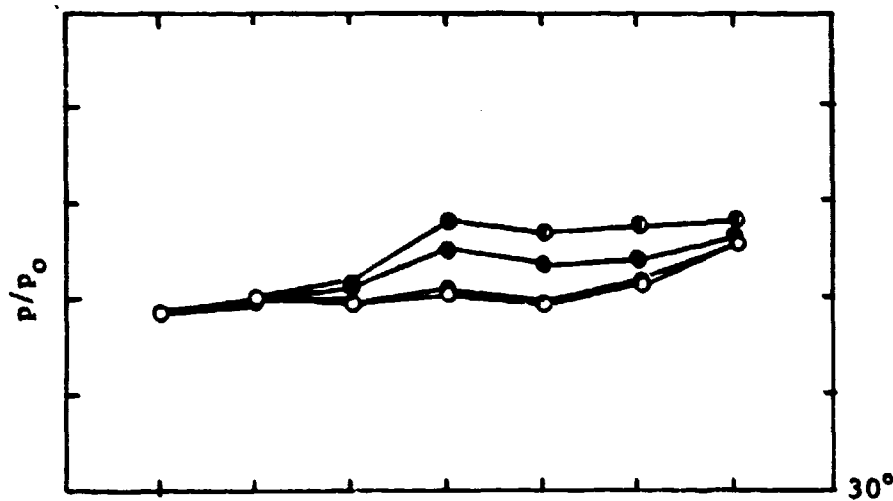
Figure 3-4. Sample output of pressure traces

Table 3-3. Summary of Torso Model Tests

Date	Shot	Incidence Angle (deg)	Peak Pressure (psi)							Free Field		Note
			P1	P2	P3	P4	P5	P6	P7	Pressure (psi)	Duration (ms)	
7-14	S-4	0	7.73	7.46	6.43	7.06	6.87	6.70	8.43	3.0	8.8	
	S-3	0	7.14	6.97	8.17	7.06	6.19	5.74	8.08	3.04	8.3	Moleskin cover
	S-5	30	6.30	6.85	6.62	6.98	6.57	7.37	8.82	3.39	8.3	
	S-6	60	3.70	4.60	6.28	6.84	5.93	6.77	5.34	3.0	8.8	
	S-7	90	4.63	3.47	3.18	4.10	4.60	5.41	8.48	3.38	8.3	
	S-1	90	4.41	3.47	3.69	4.38	4.23	4.74	7.60	3.00	8.6	Repeat
	S-2	90	5.71	3.75	3.69	4.38	4.23	4.18	8.82	3.04	8.6	Moleskin cover
	S-4	90	4.91	3.47	3.06	4.01	4.60	4.74	7.60	3.43	8.6	Moleskin surface
7-14	S-8	120	4.63	4.20	3.18	3.13	2.96	3.98	5.65	3.61	8.4	
	S-9	150	7.40	3.79	3.35	3.20	2.44	2.63	8.64	3.69	8.4	
	S-10	180	8.41	3.23	3.35	3.28	2.82	3.10	8.48	3.84	8.3	
7-14	S-11	0	13.29	13.56	10.71	11.91	11.71	11.54	12.40	5.61	8.0	
	S-12	30	10.51	11.38	11.30	12.12	11.33	12.56	14.37	5.69	7.8	
	S-13	60	5.39	7.26	8.62	10.04	9.34	11.38	8.87	5.23	8.1	
	S-14	90	7.57	6.46	4.60	6.02	6.82	7.64	13.42	5.54	7.6	
	S-15	120	6.31	5.73	4.60	4.54	4.67	6.21	9.03	5.54	7.4	
	S-16	150	8.07	5.65	4.69	4.54	3.71	3.18	13.11	5.38	7.5	
	S-17	180	12.87	4.20	4.77	5.05	4.67	4.54	13.11	5.54	7.6	
7-14	S-18	0	24.16	26.21	21.34	24.34	23.70	22.09	26.08	9.62	6.7	
7-15	S-8	0	21.01	23.79	27.20	33.46	28.89	23.49	25.10	9.42	6.9	Moleskin cover
7-14	S-19	30	17.02	17.74	19.66	23.23	21.48	22.28	24.51	9.04	6.3	
7-15	S-1	60	10.08	12.10	14.23	17.10	17.97	20.90	16.86	7.88	7.2	
	S-3	90	18.49	10.28	10.04	10.60	10.37	16.72	32.55	8.08	6.8	Moleskin cover
	S-4	90	14.71	11.09	8.37	10.23	11.48	15.91	27.45	8.27	7.0	
	S-5	120	13.03	10.08	6.49	7.62	8.52	12.14	17.65	8.27	6.9	
	S-6	150	19.96	11.29	7.95	6.69	4.81	7.96	26.67	8.65	7.4	
	S-7	180	28.36	8.67	7.32	8.36	7.04	6.56	26.08	8.84	6.2	
	S-16	0	63.87	80.66	69.04	80.69	81.84	64.67	80.79	26.92	3.6	
7-15	S-15	0	84.04	88.73	86.61	105.2	106.6	76.80	82.36	31.15	3.7	Repeat
	S-14	30	56.73	45.57	66.94	86.63	83.69	84.80	87.46	30.38	3.9	
	S-13	60	31.94	18.15	37.66	49.08	57.40	79.60	57.26	24.61	4.1	
	S-9	90	48.32	18.15	22.18	27.88	31.85	65.67	85.50	21.15	3.9	
	S-10	120	31.94	20.17	15.90	19.34	23.32	42.98	47.06	23.00	4.0	
	S-11	150	55.89	20.17	16.32	12.27	13.33	16.31	77.26	24.61	3.3	
	S-12	180	46.22	15.33	15.90	13.38	8.89	11.94	48.24	22.31	4.1	

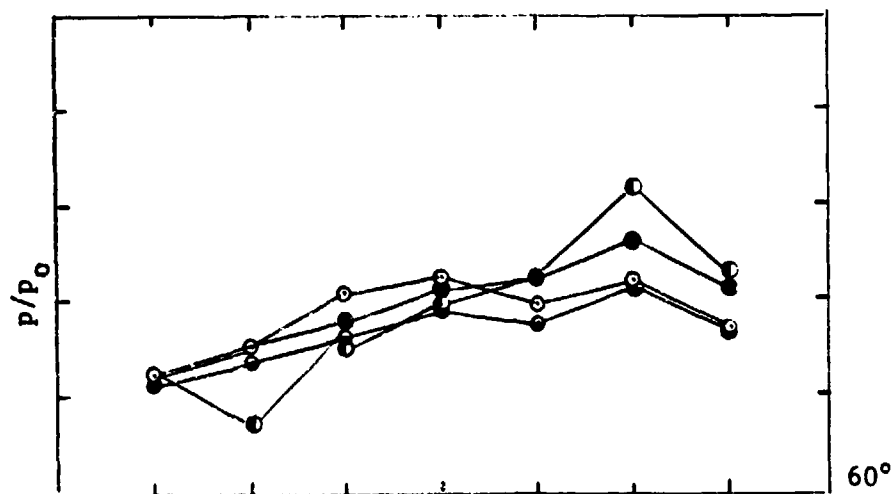


a. 0° (o: 3.0 psi; e: 5.61 psi; e: 9.62 psi; e: 26.92 psi)

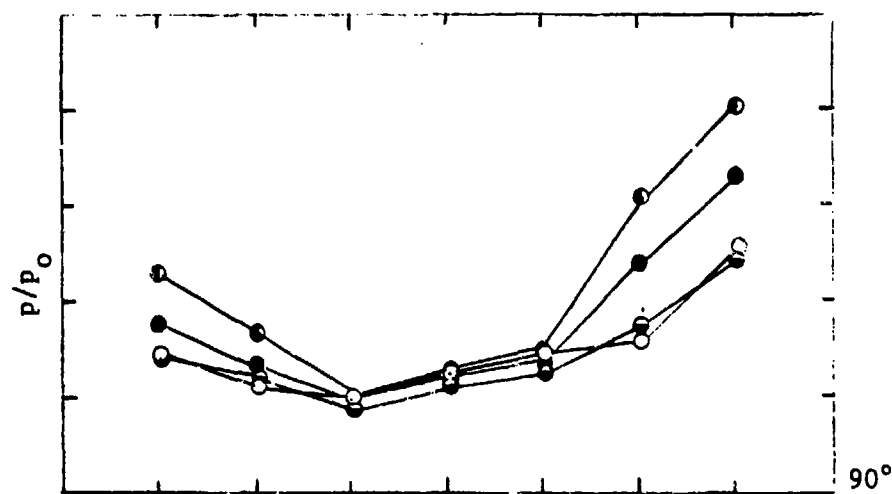


b. 30° (o: 3.39 psi; e: 5.69 psi; e: 9.04 psi; e: 30.38 psi)

Figure 3-5. Pressure coefficient around the torso model

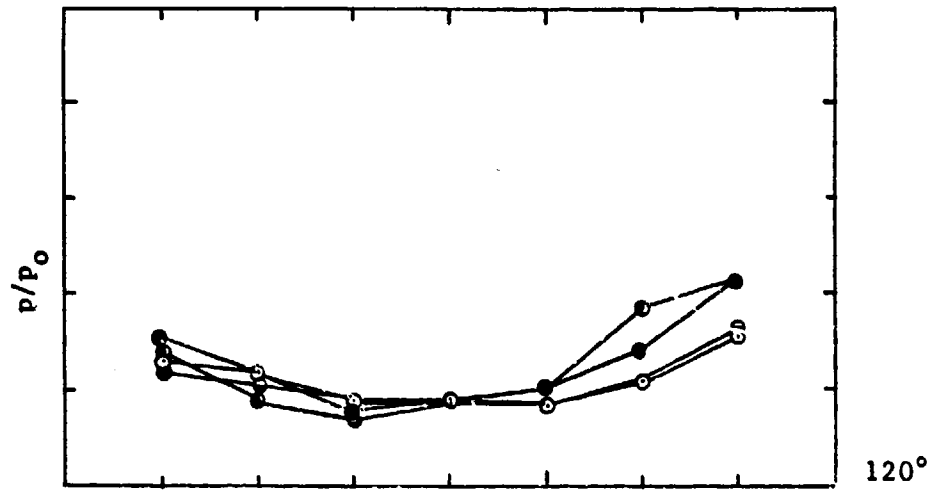


c. 60° (o: 3.0 psi; •: 5.23 psi; ■: 7.88 psi; ♦: 24.61 psi)

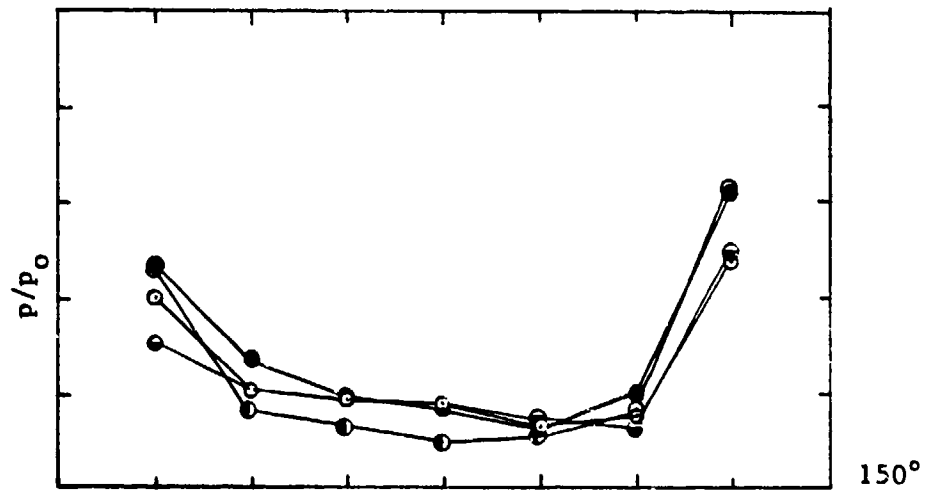


d. 90° (o: 3.19 psi; •: 5.54 psi; ■: 8.27 psi; ♦: 21.15 psi)

Figure 3-5. (Cont'd).

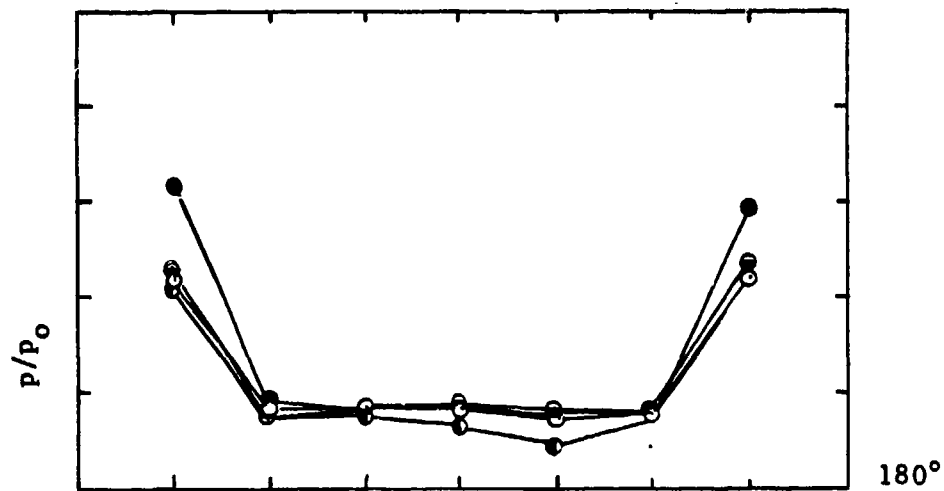


e. 120° (o: 3.61 psi; •: 5.54 psi; ■: 8.27 psi; ♦: 22.0 psi)



f. 150° (o: 3.69 psi; •: 5.38 psi; ■: 8.65 psi; ♦: 24.61 psi)

Figure 3-5. (Cont'd).



g. 180° (○: 3.84 psi; ●: 5.54 psi; ◐: 8.84 psi; ●: 22.31 psi)

Figure 3-5. (Cont'd).

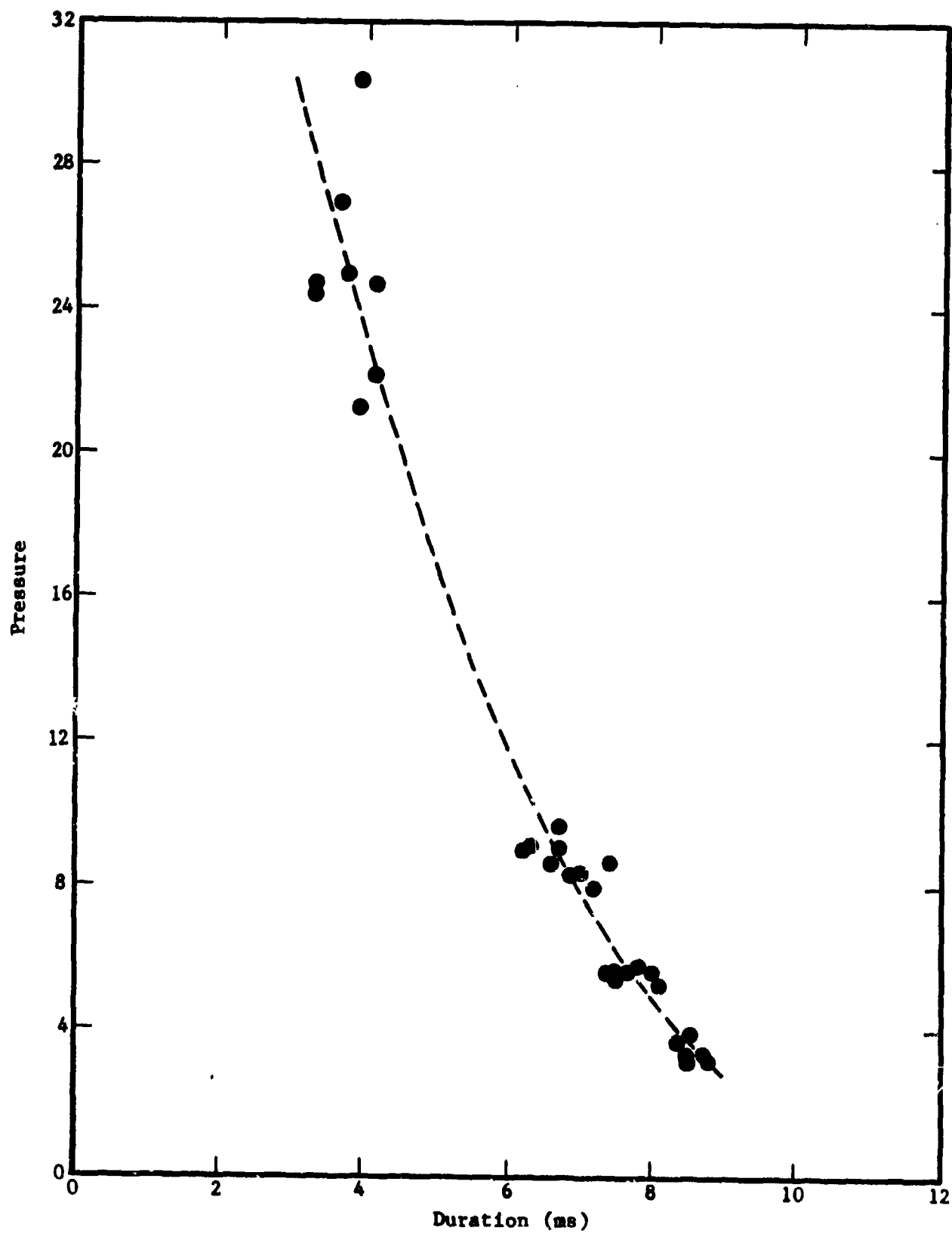
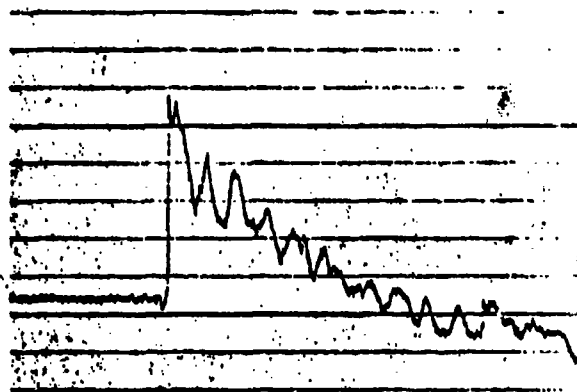
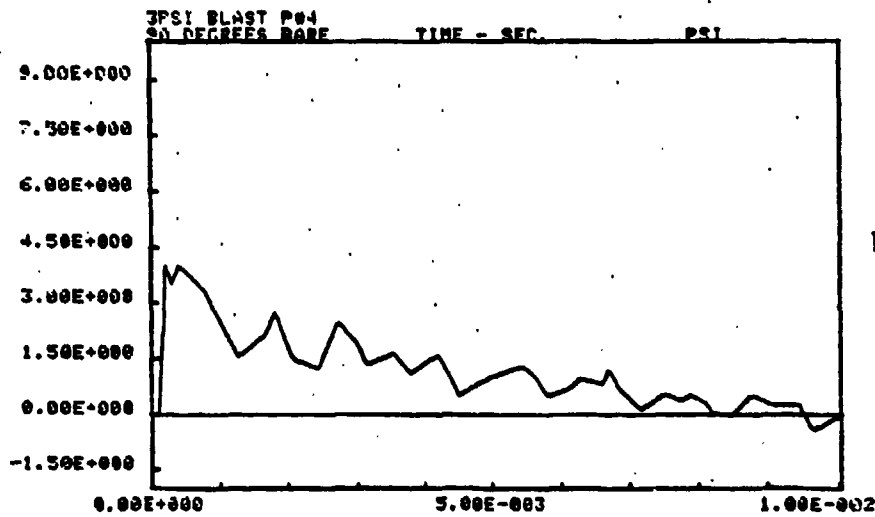


Figure 3-6. Free field peak pressure vs. A-duration



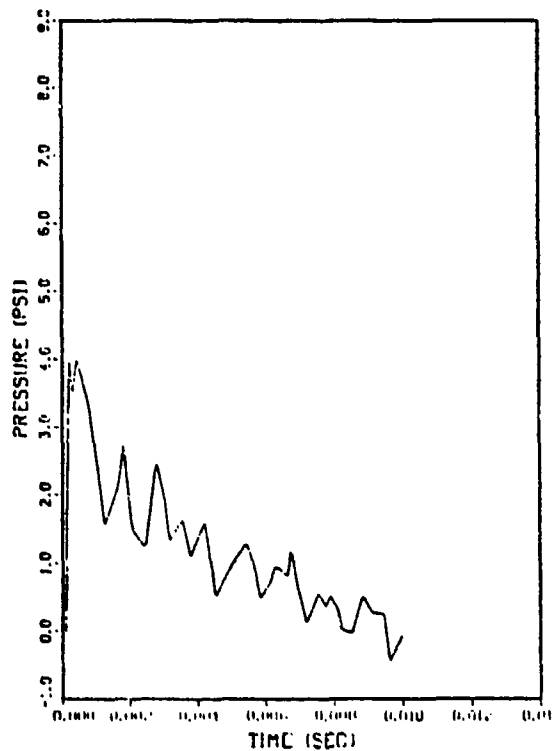
a. Data Trace

IS THIS O.K.?



b. Texttronix
Digitizer Output

3PSI BLAST P#4 90 DEGREES



c. Computer Plot

Figure 3-7. Comparison of digitized signal with probe output

4. COMPARISON WITH EITACC CALCULATIONS

The objectives of this work are to demonstrate that a computer code can calculate the loading due to a blast wave and to determine properties of the loading that can be used in the biomechanical analysis.

4.1 DESCRIPTION OF THE EITACC CODE

EITACC is a JAYCOR developed general purpose computer code for the calculation of multi-dimensional, time-dependent, one- and two-phase flows. It can be used for either compressible or incompressible flow. The code has undergone extensive validation and verification procedures to assure its reliability in a variety of applications. In the present study, the two-dimensional, single phase, compressible version of the code has been used to analyze the experiments described in the previous sections.

A computational mesh was chosen with 102 cells of constant spacing 0.015 m along the direction of propagation of the wave and 22 lateral cells with spacings of 0.05 m. The torso and arms of the body were modeled using partial cell blockages to simulate the actual geometry. The pressure-time variation at the probe locations were computed and compared with the output from the experimental data. Impulse loadings for both experiment and calculation were compared.

The size of the mesh spacings has an important effect on the calculated pressure traces. Because of the finite cell sizes required in the computation, some of the very sharp pressure spikes are rounded off. The details of the pressure history can be captured only by using extremely fine spatial resolution. However, the general features of the loading and the total impulse can be obtained with moderate resolution and the mesh sizes and time steps used in these calculations appear to resolve the pressure-time histories for most of the probe locations.

The measured free-field blast pressure time history is used as the inlet boundary condition. The other computational boundaries at the sides and outlet

downstream from the body use radiation pressure boundary conditions to reduce wave reflection. Initially the gas is at rest. The EITACC code solves the transient gas dynamics equations subject to these initial and boundary conditions.

4.2 PROPAGATION OF BLAST WAVES

In the EITACC calculations, the experimental blast data are simulated by inlet pressure boundary conditions. For each experiment, the maximum blast inlet pressure and pulse duration time, A-duration time, are used. In any finite difference simulation of the blast wave propagation there is some distortion of the wave as it moves through the computational mesh.

Three calculations were made with EITACC to study its effect on wave propagation. These calculations were made with peak pressures of 5.61, 9.62, and 26.92 psi, and A-duration times of 8, 6.7, and 3.6 msec, respectively. The computational mesh was comprised of 102 cells in the y-direction, with equal spacings of 0.015 m, and 4 cells in the x-direction with spacings of 0.05 m. No blockage due to a body was included.

Figure 4-1 shows the spatial variation of the 5.61 psi wave as it moves through the computational mesh. In later calculations the body will be located approximately 0.75 m from the inlet. From Figure 4-1 we can see that the 5.61 psi wave would reach the body in about 2 msec and retains its shape and magnitude. Numerical smearing of the wave is limited to the front face. There is some reflection off the outlet boundary that will reach the body by 6 msec. By that time the significant part of the loading is over. Figures 4-2 and 4-3 show that the 9.62 and 26.92 psi waves also retain their inlet pressure wave shapes and magnitudes. The higher pressure waves move more rapidly, and in the case of the 26.92 psi wave, impact with the body would occur at about 1.5 msec.

These calculations imply that the finite difference numerical schemes used in EITACC are sufficiently accurate to follow the detailed blast wave propagation in the experiments.

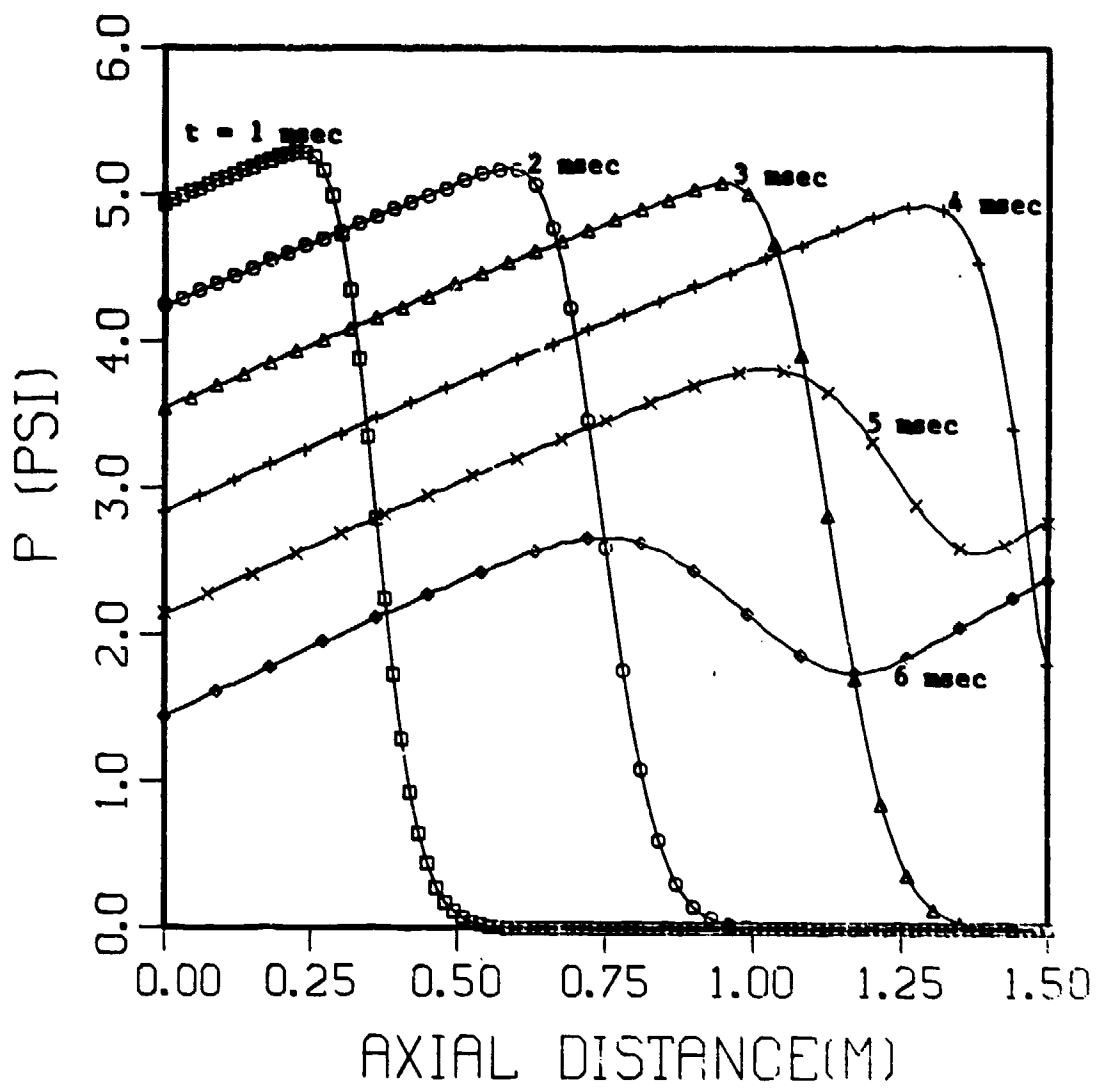


Figure 4-1. 5.61 psi pressure wave propagation as a function of time

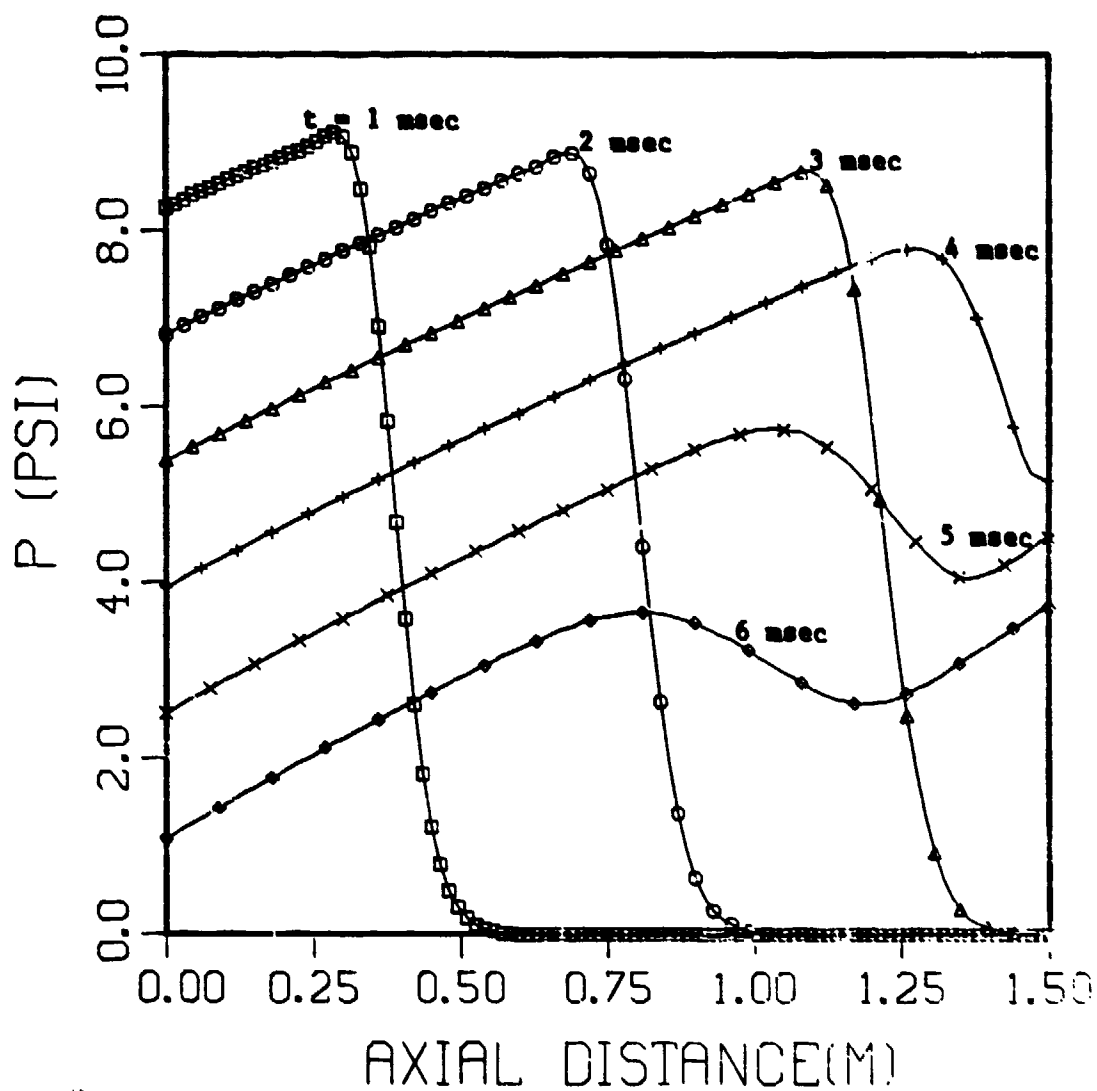


Figure 4-2. 9.62 psi pressure wave propagation as a function of time

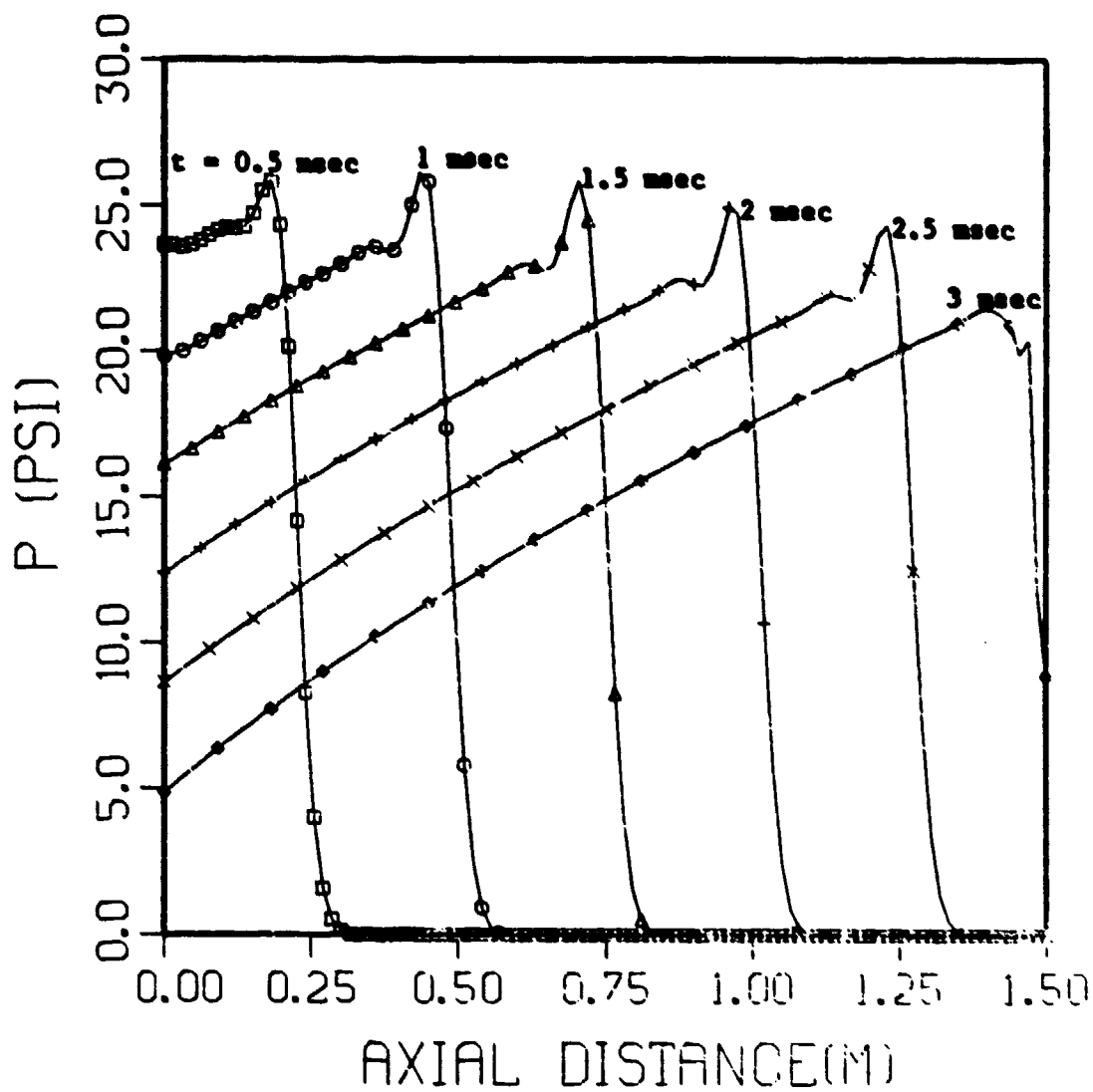


Figure 4-3. 26.92 psi pressure wave propagation as a function of time

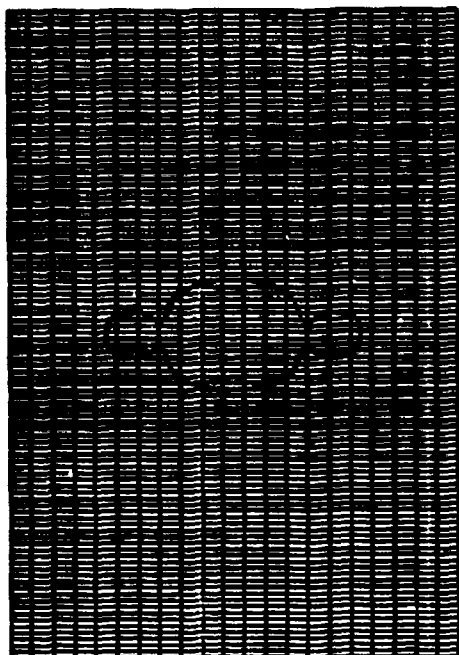
4.3 LOADING FOR A NOMINAL 3 PSI WAVE

The dimensions of the physical model were used in the EITACC calculations. Pressure signals from the cells corresponding to the probe locations were then calculated and printed. Additionally, a computational cell located between the center of the arm and the boundary and in front of the body was used to determine the reference pressure. For each time step, pressure contours and velocity vectors were calculated. Impulses at every probe cell were then obtained by summing the products of the pressure and the time step up to the time when a negative pressure was calculated. Similarly, experimental pressure data and impulse information were also computed for comparison with the calculations.

Typical plots showing the computational mesh, with the body in place, for tests at 0° , 30° , 60° , and 90° , respectively, are shown in Figure 4-4(a)-(d). Figures 4-5(a)-(c) and 4-6(a)-(c) show typical calculated velocity vector plots and pressure contour plots out to 10 msec for the 3 psi, 0° calculation. Similar velocity vector and pressure contour plots showing interaction of the wave with the body are presented in Figures 4-7 through 4-12 for body orientations of 30° , 60° and 90° with the incoming nominal 3 psi blast wave.

Figure 4-13 compares calculated and measured pressure traces for the 3.0 psi $\theta = 0^\circ$ experiment. The solid line calculated pressure traces are shown for the seven probes along the front of the body and for two probes behind the body. A location away from the body is shown in the upper left corner plot and is compared with the free-field experimental value. The experimental data for the various probes has been offset approximately 2 msec to correspond to the arrival of the blast wave at the body. As expected, due to the smoothing effect of the finite cell size, the sharp peak values are reduced. The pressure traces are distorted in regions where the signals vary rapidly, as in the space between the arm and the body, but agree well at other locations.

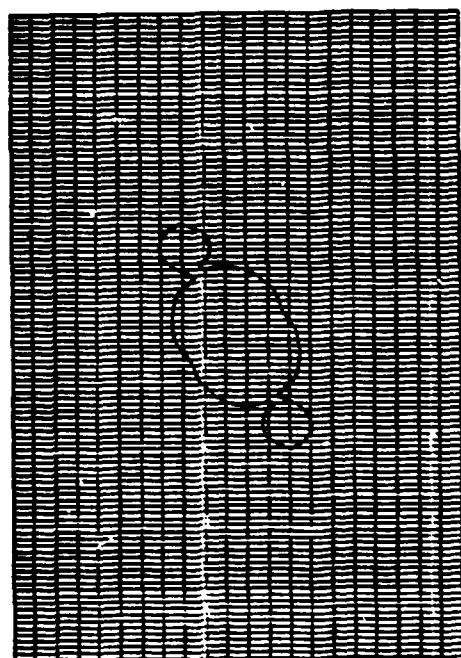
Figures 4-14 through 4-19 compare calculated and measured probe and free field data for 3 psi waves at other orientations from $\theta = 30^\circ$ to 180° . There is general agreement between calculation and measurement, except in the arm regions.



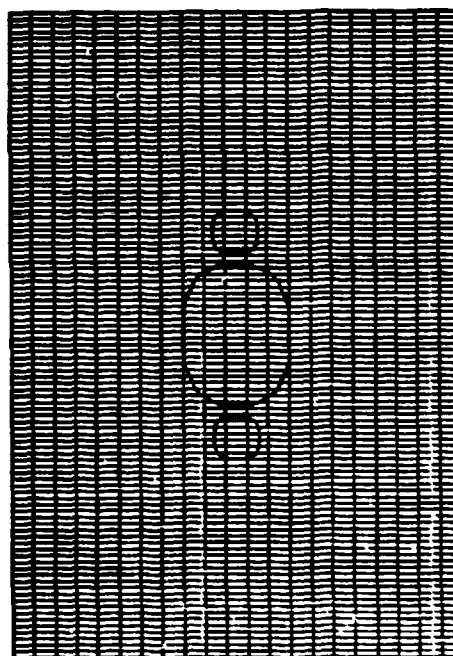
(a) 0°



(b) 30°



(c) 60°



(d) 90°

Figure 4-4. Computational mesh plots for 9-90° calculations

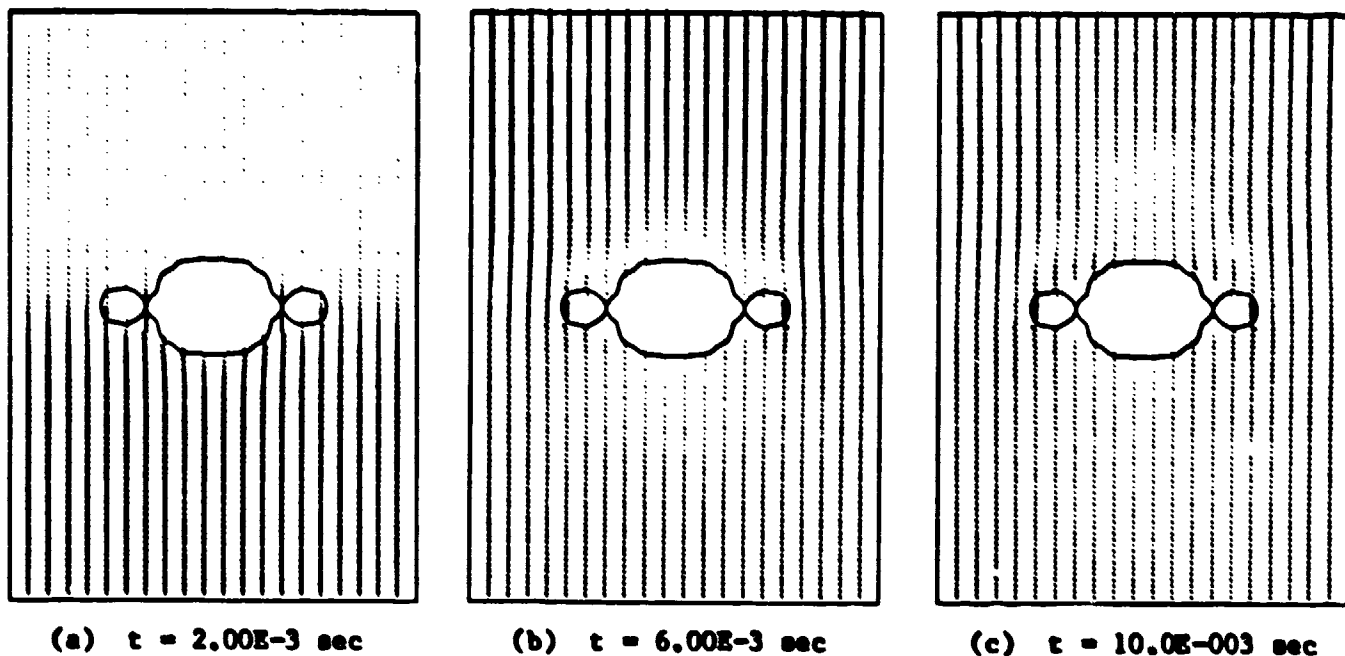


Figure 4-5. Vector plots at 0° , 3.0 psi

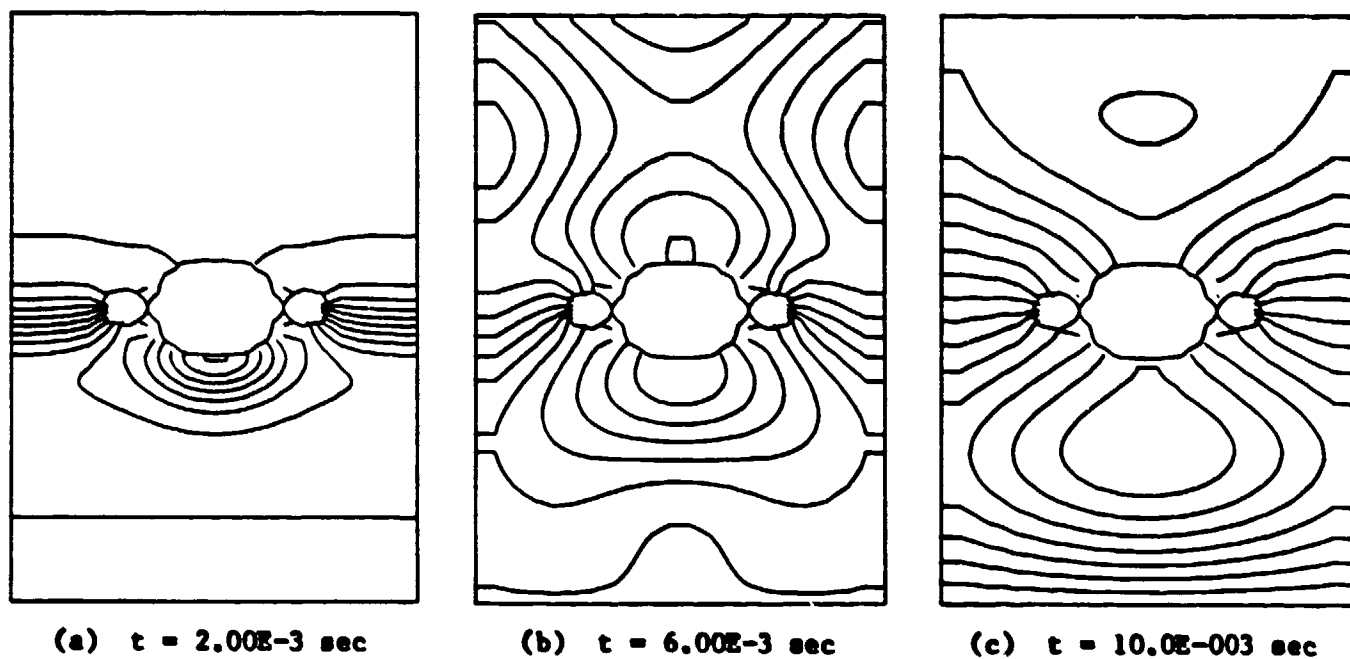
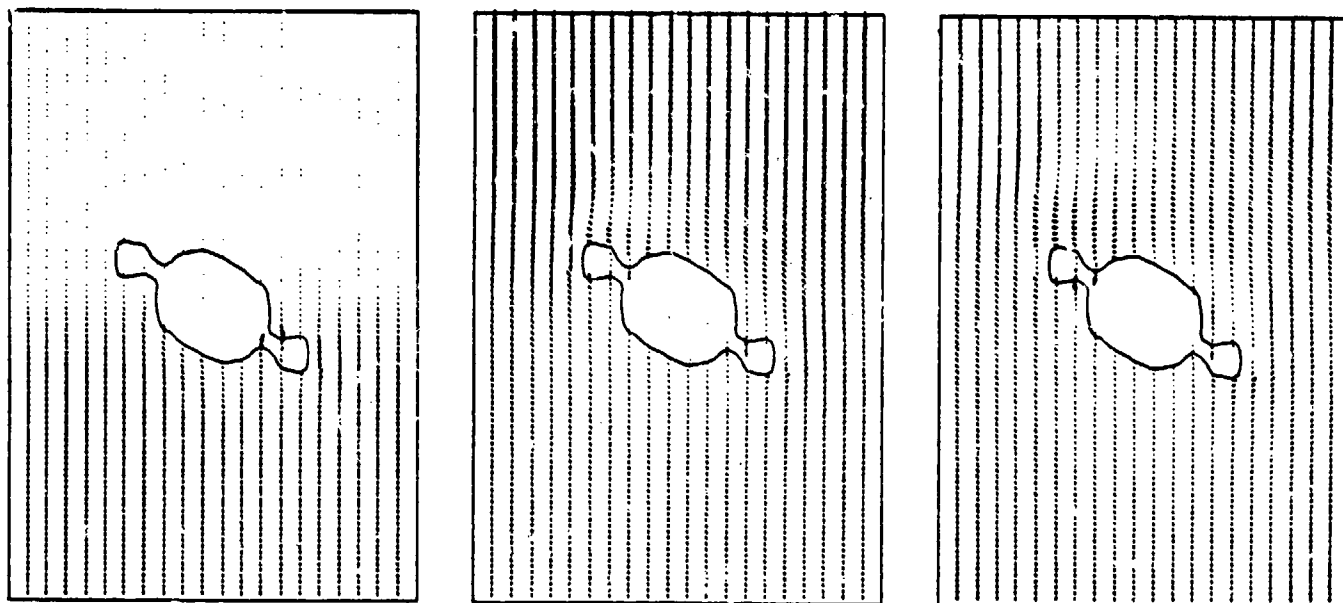


Figure 4-6. Pressure contours at 0° , 3.0 psi

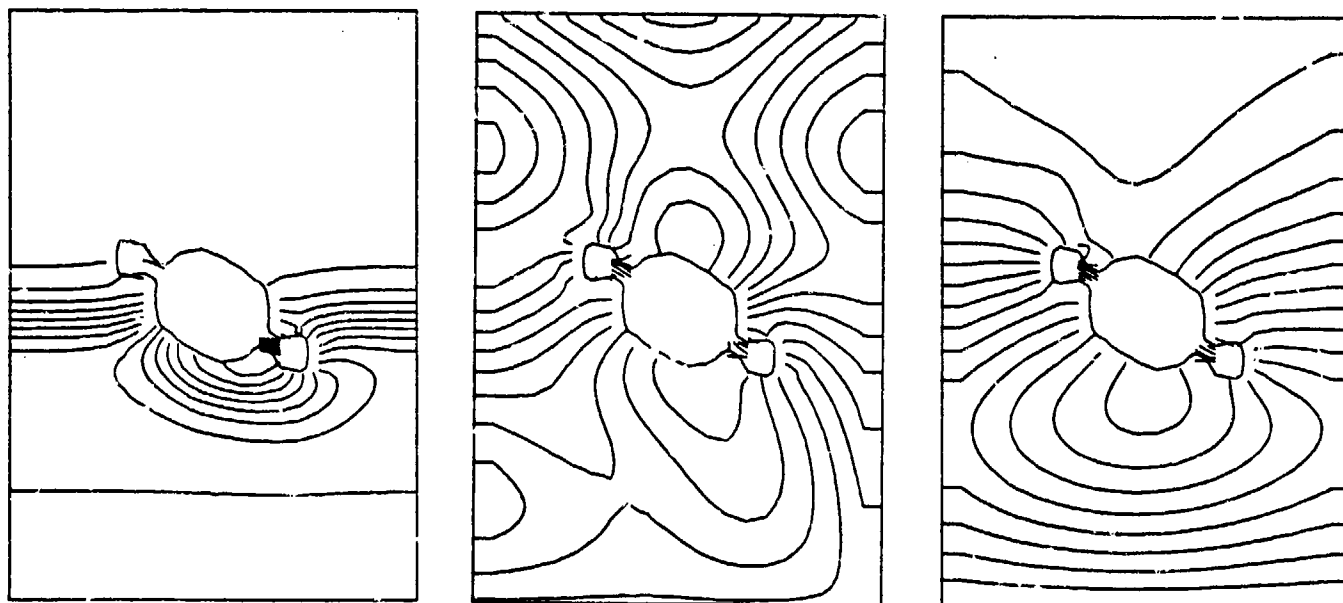


(a) $t = 2.00E-3$ sec

(b) $t = 6.00E-3$ sec

(c) $t = 10.0E-003$ sec

Figure 4-7. Vector plots at 30° , 3.39 psi

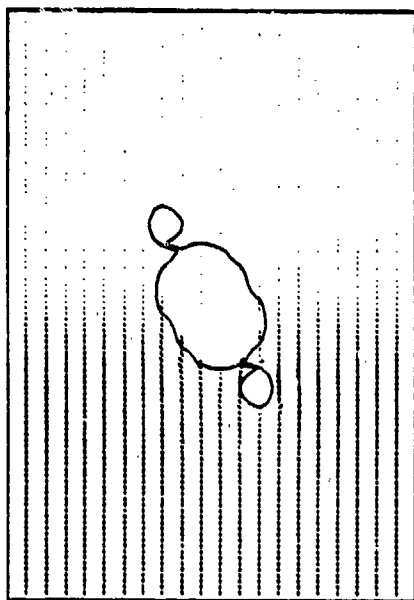


(a) $t = 2.00E-3$ sec

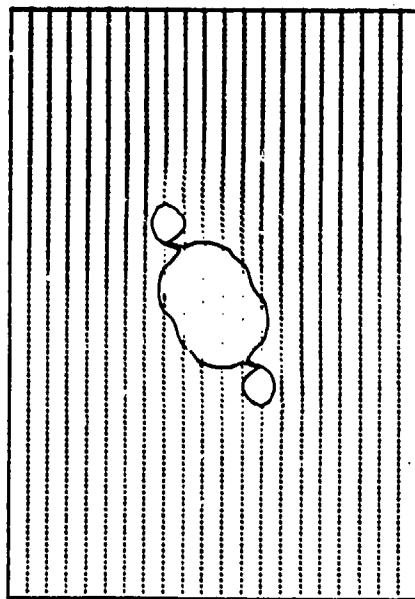
(b) $t = 6.00E-3$ sec

(c) $t = 10.0E-003$ sec

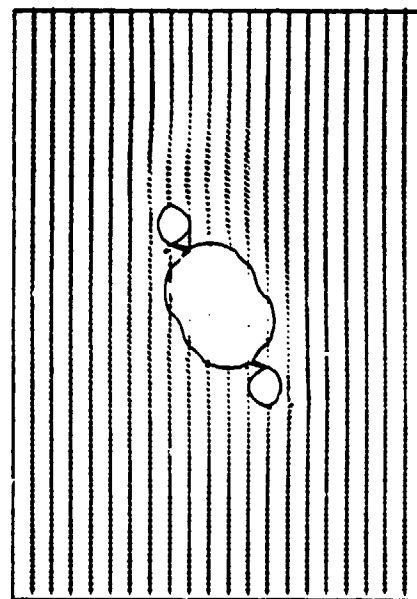
Figure 4-8. Pressure contours at 30° , 3.39 psi



(a) $t = 2.00E-3$ sec

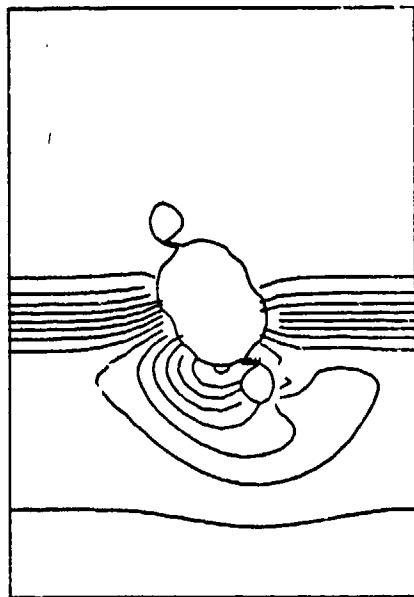


(b) $t = 6.00E-3$ sec

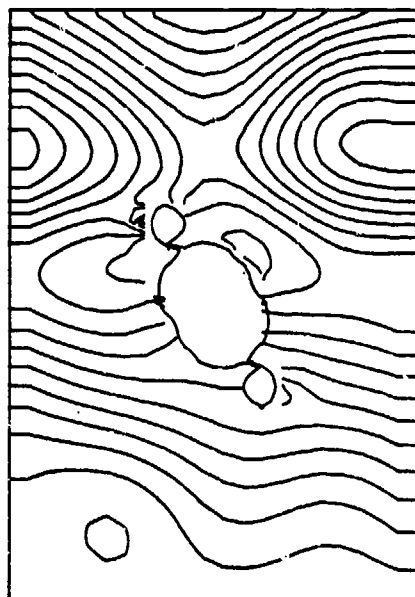


(c) $t = 10.0E-003$ sec

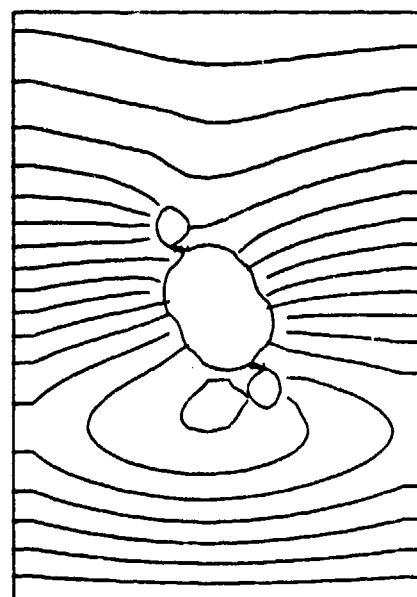
Figure 4-9. Vector plots at 60° , 3.0 psi



(a) $t = 2.00E-3$ sec

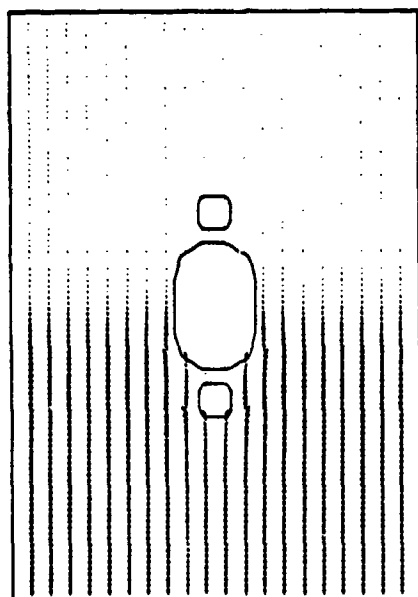


(b) $t = 6.00E-3$ sec

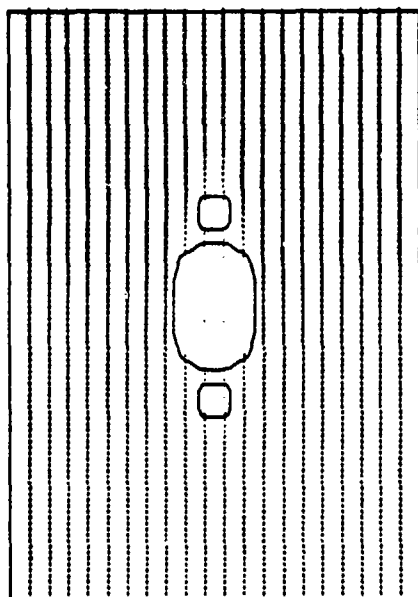


(c) $t = 10.0E-003$ sec

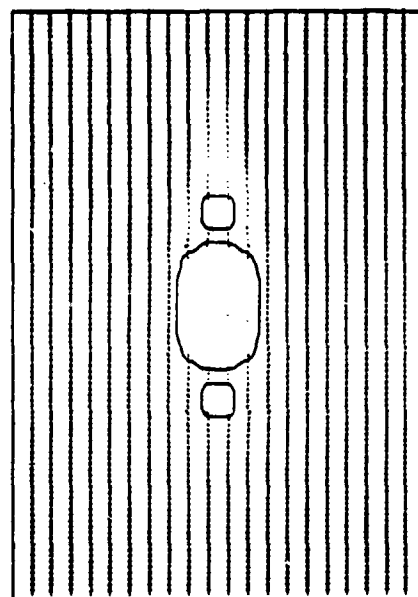
Figure 4-10. Pressure contours at 60° , 3.0 psi



(a) $t = 2.00E-3$ sec

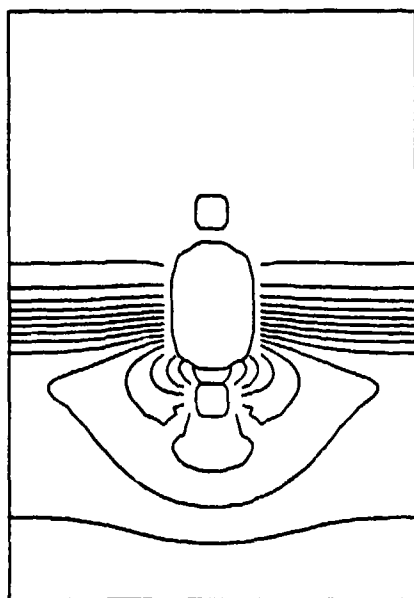


(b) $t = 6.00E-3$ sec

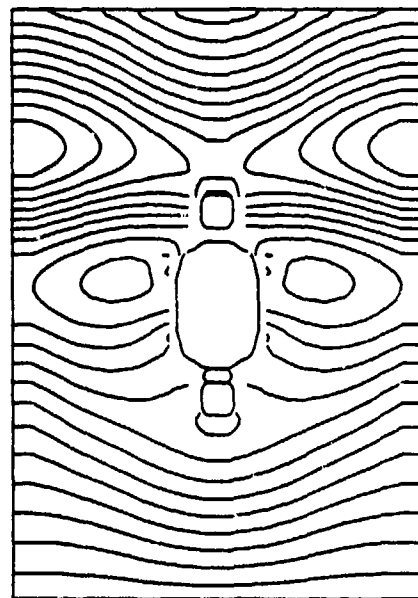


(c) $t = 10.0E-003$ sec

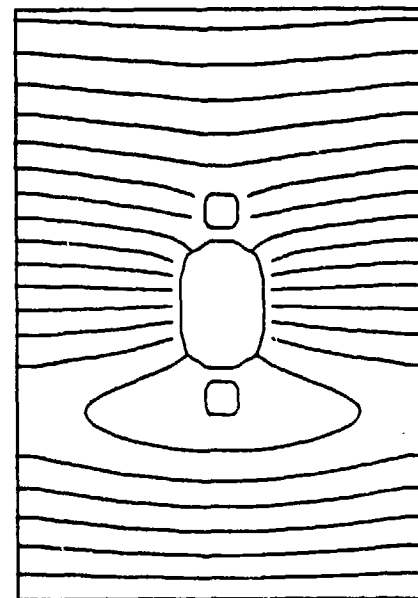
Figure 4-11. Vector plots at 90° , 3.38 psi



(a) $t = 2.00E-3$ sec



(b) $t = 6.00E-3$ sec



(c) $t = 10.0E-003$ sec

Figure 4-12. Pressure contours at 90° , 3.38 psi

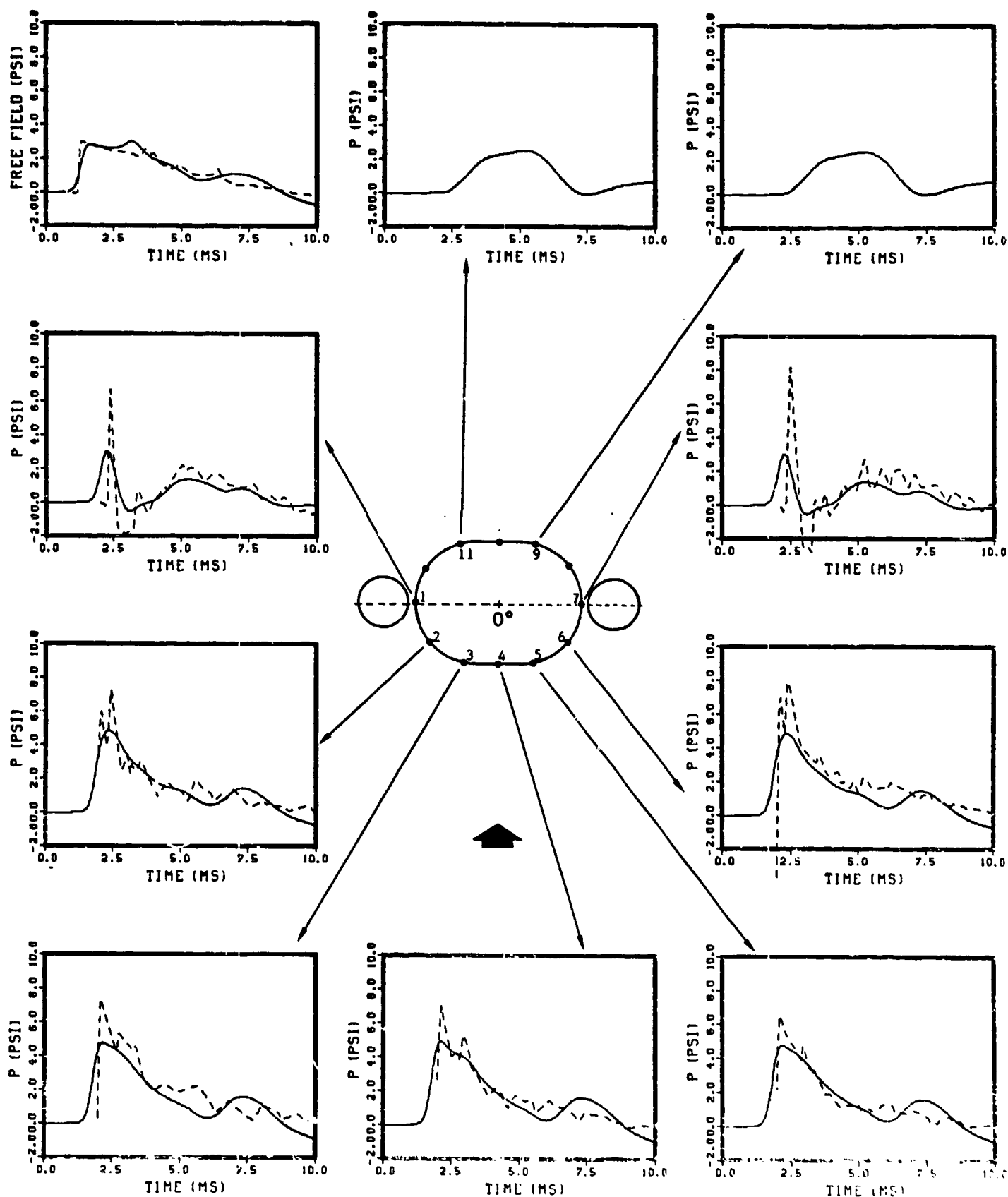


Figure 4-13. Comparison of calculated (—) and measured (---) pressure signals for free field and probes. 3 psi wave, $\theta = 0^\circ$.

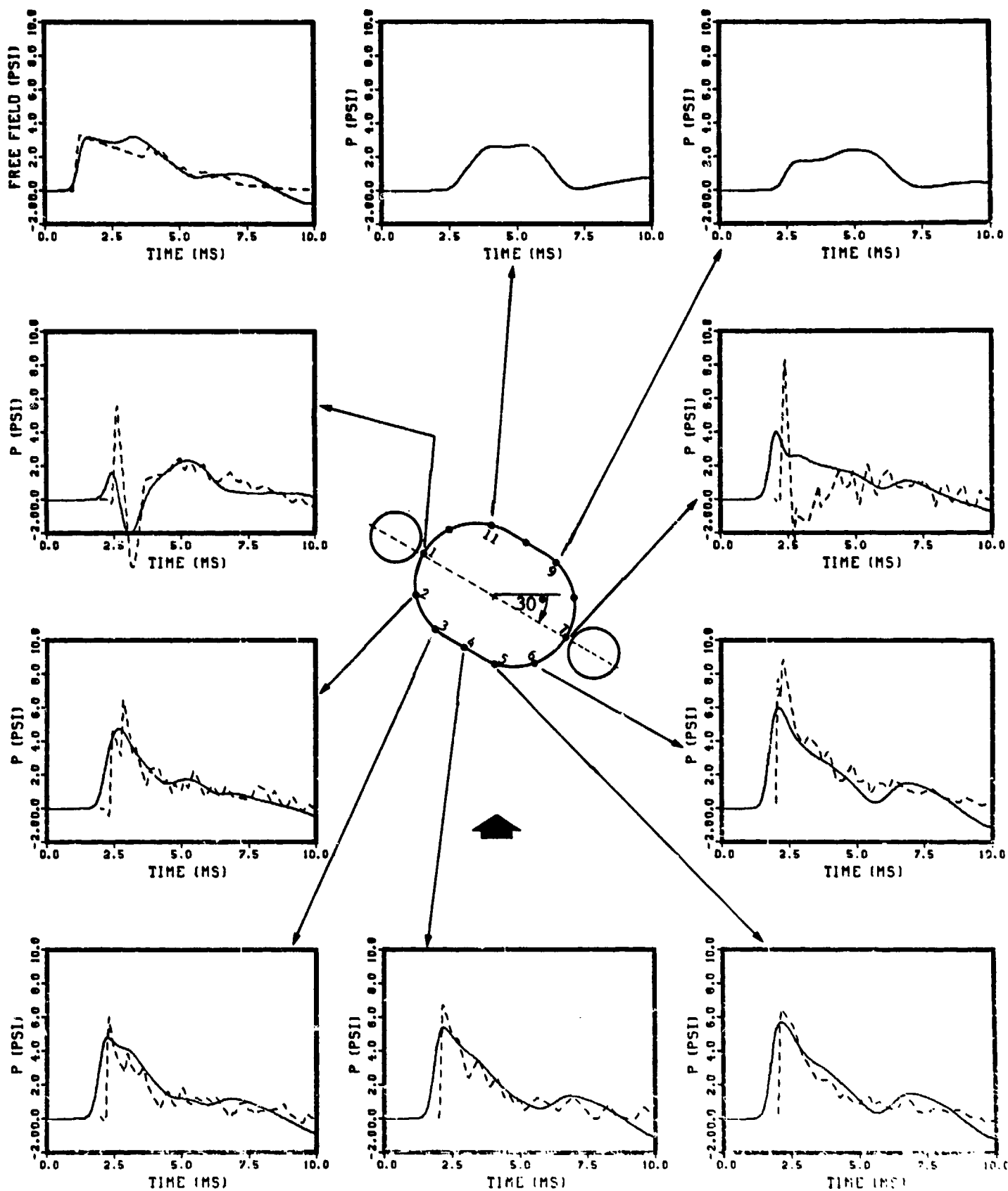


Figure 4-14. Comparison of calculated (—) and measured (---) pressure signals for free field and probes. 3.39 psi wave, $\theta = 30^\circ$.

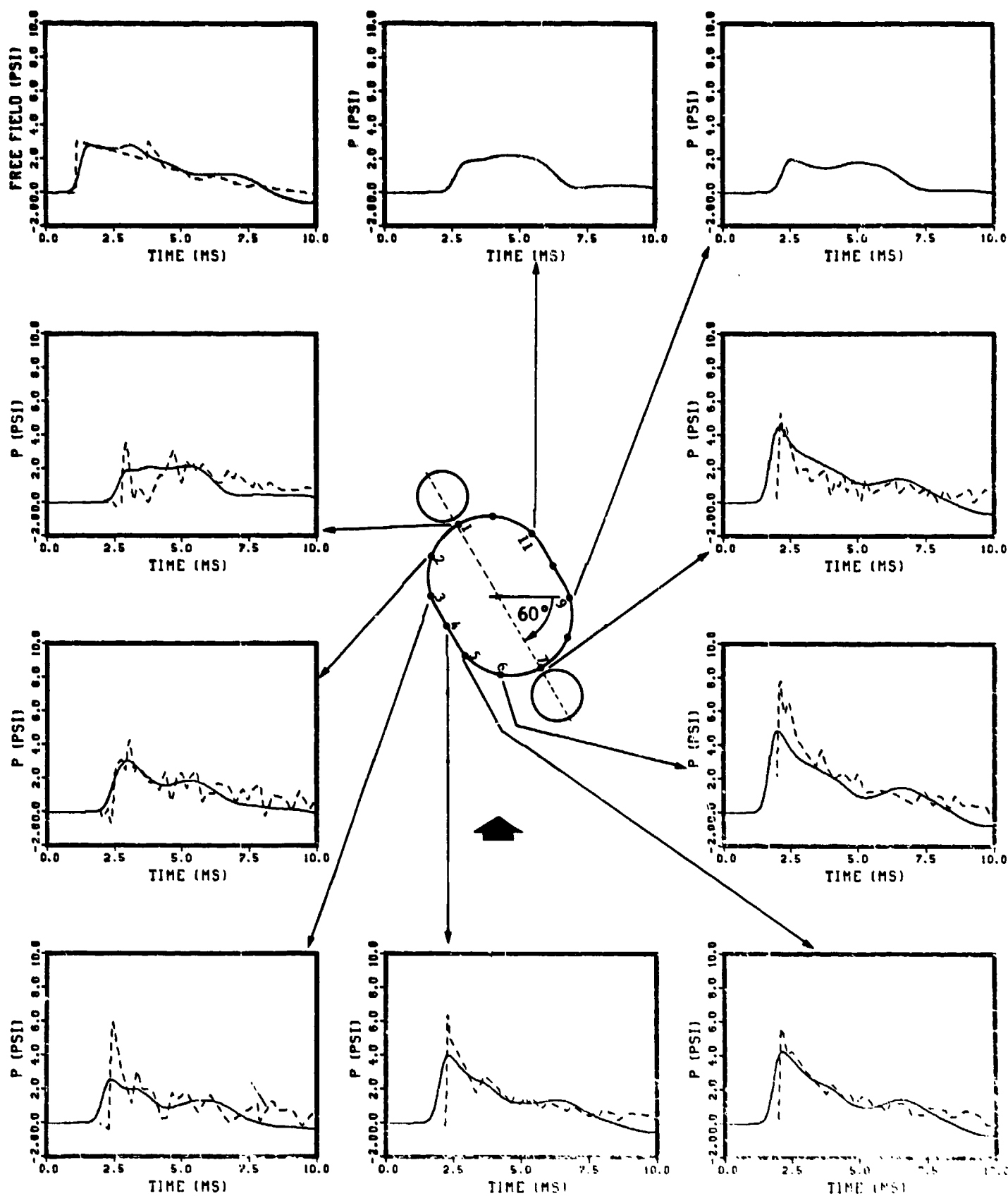


Figure 4-15. Comparison of calculated (—) and measured (---) pressure signals for free field and probes. 3.0 psi wave, $\theta = 60^\circ$.

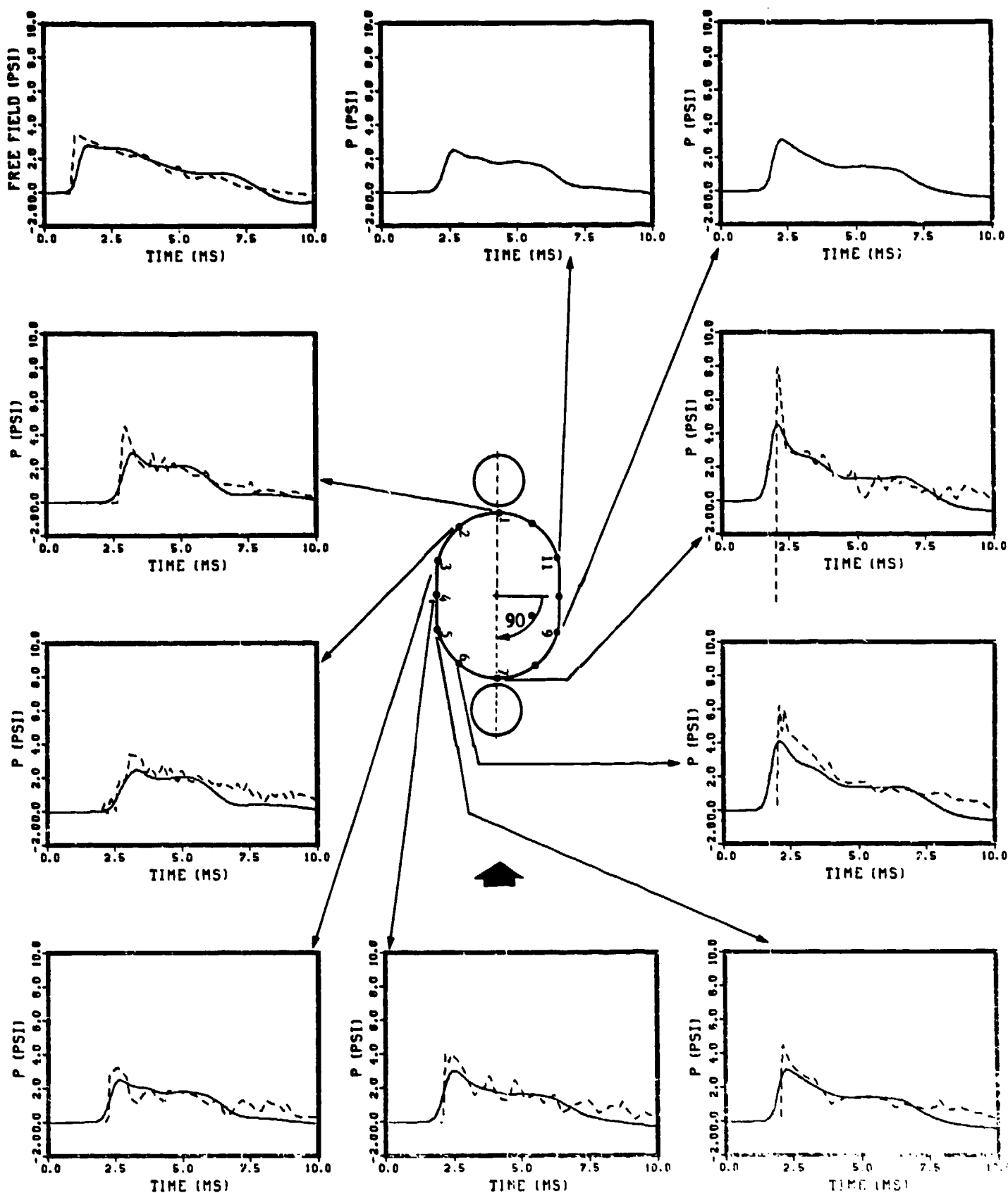


Figure 4-16. Comparison of calculated (—) and measured (---) pressure signals for free field and probes. 3.38 psi wave, $\theta = 90^\circ$.

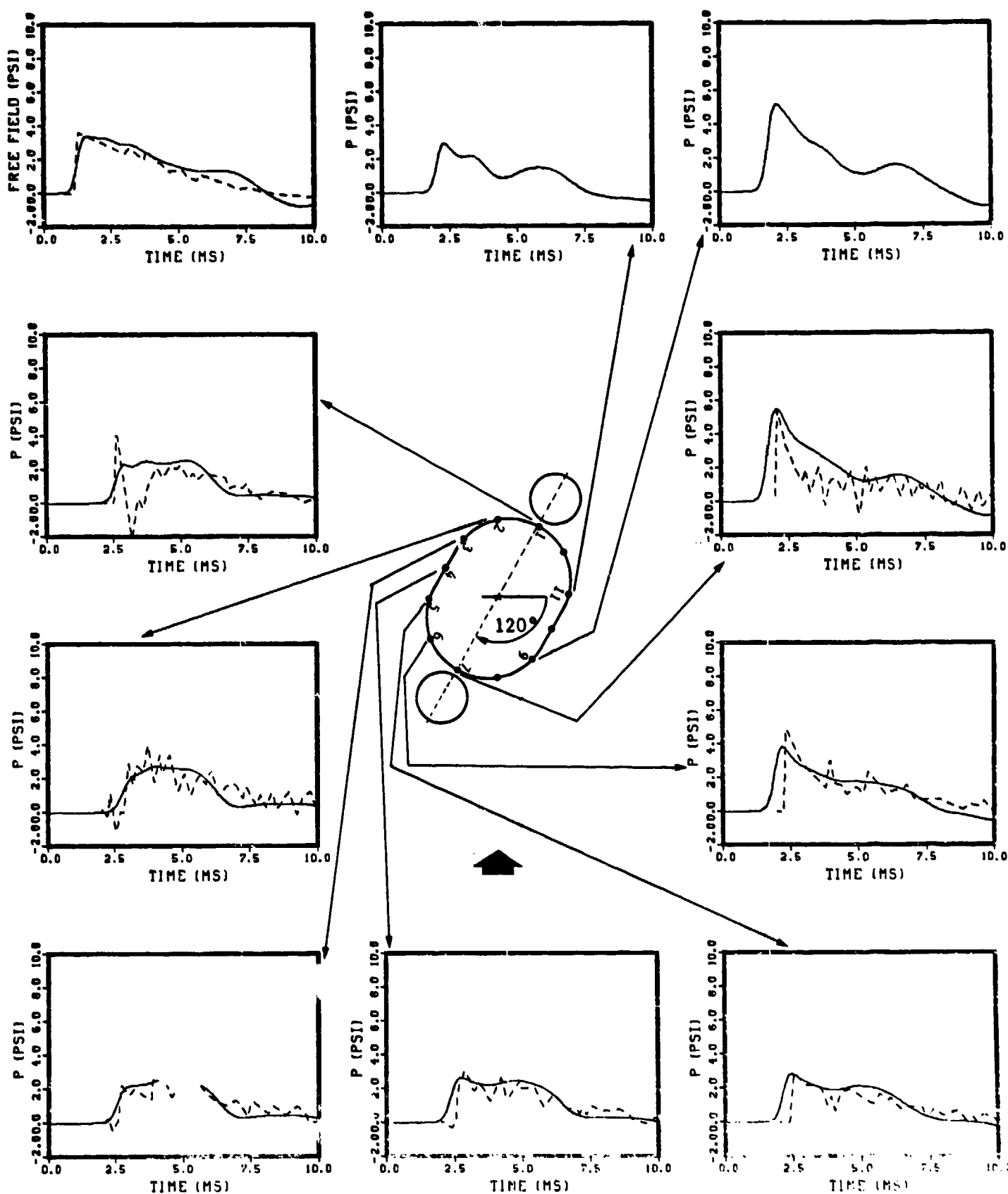


Figure 4-17. Comparison of calculated (—) and measured (---) pressure signals for free field and probes. 3.61 psi wave, $\theta = 120^\circ$.

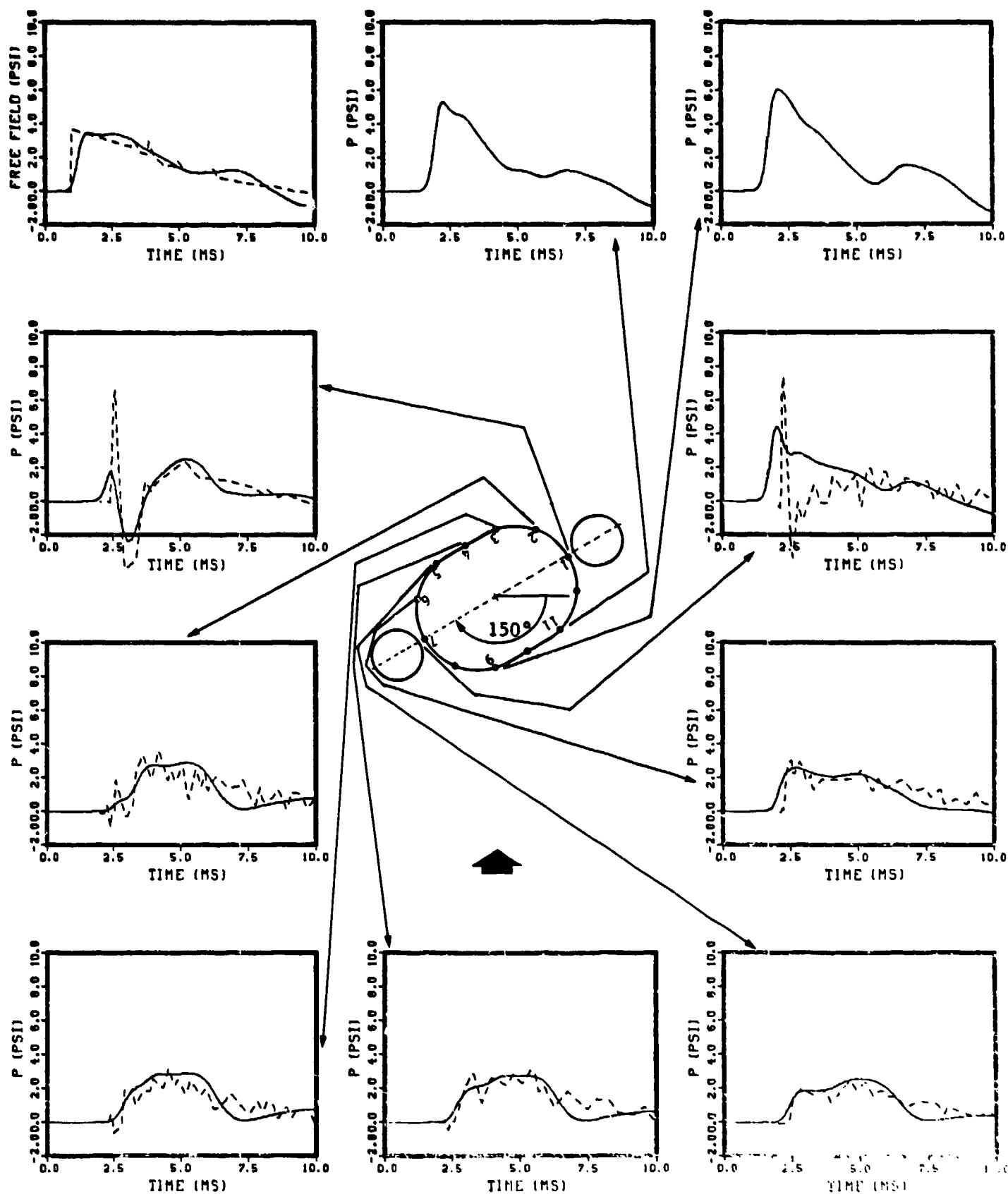


Figure 4-18. Comparison of calculated (—) and measured (---) pressure signals for free field and probes. 3.69 psi wave, $\theta = 150^\circ$.

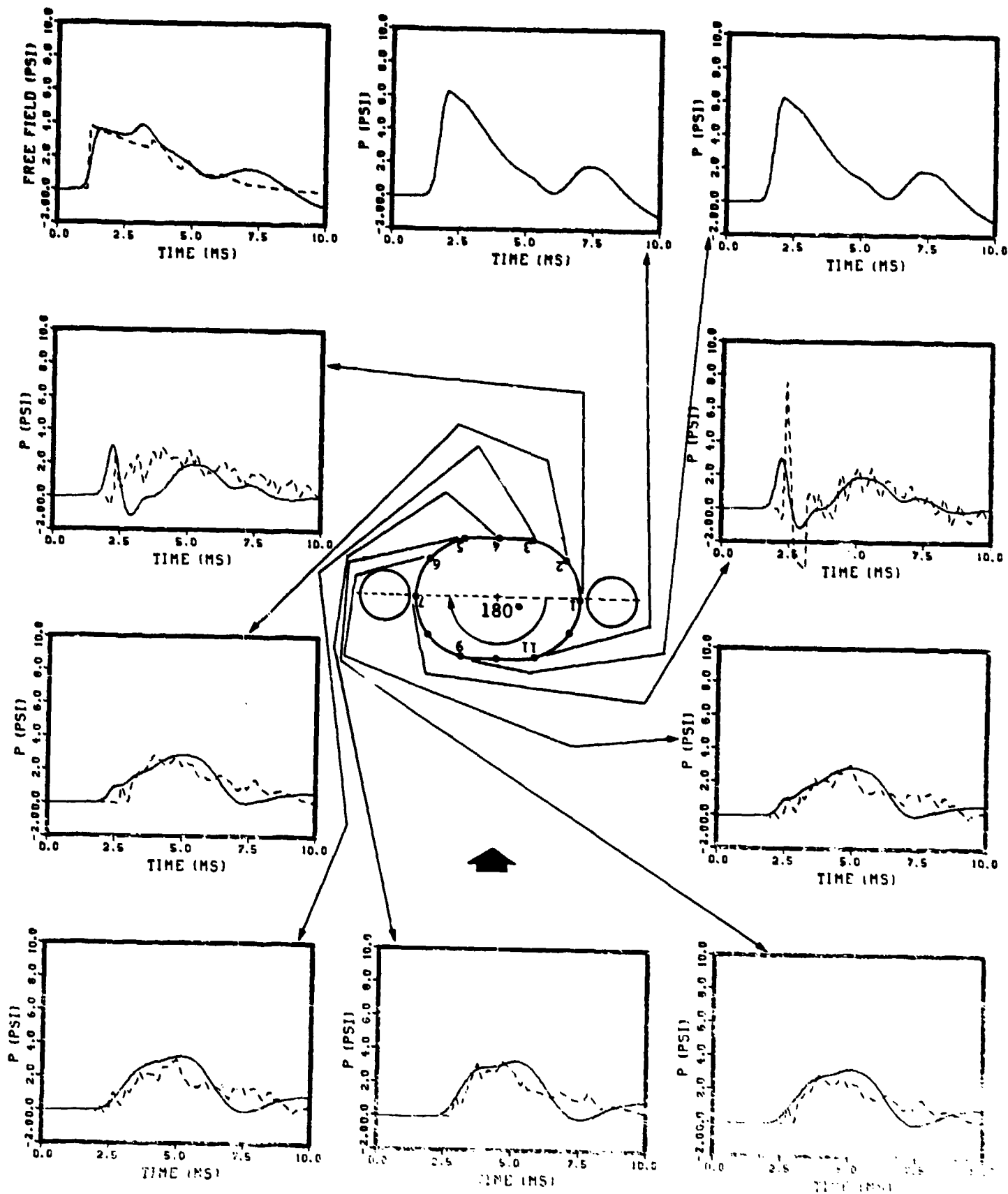


Figure 4-19. Comparison of calculated (—) and measured (---) pressure signals for free field and probes. 3.04 psi wave, $\theta = 180^\circ$.

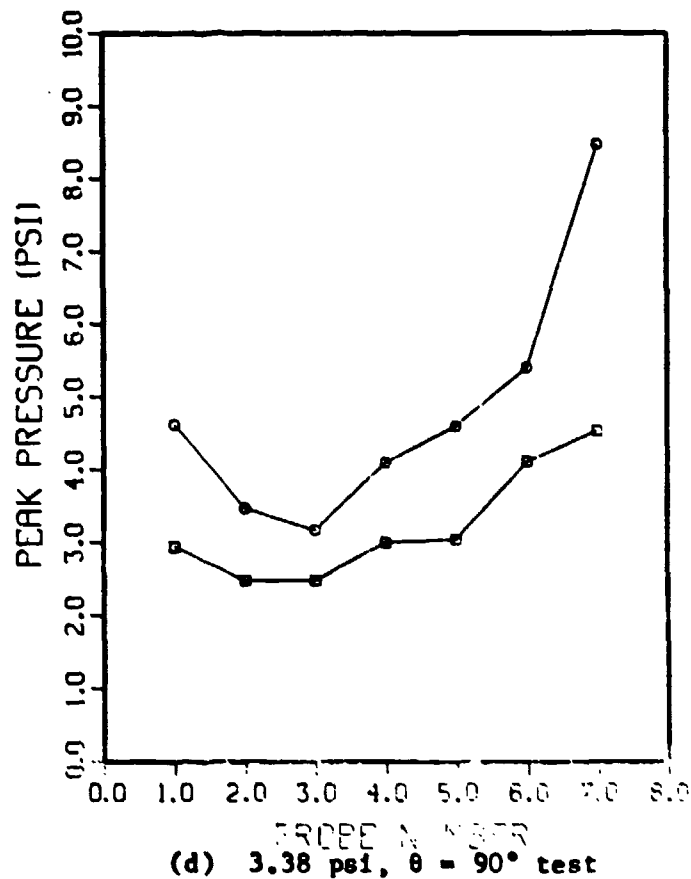
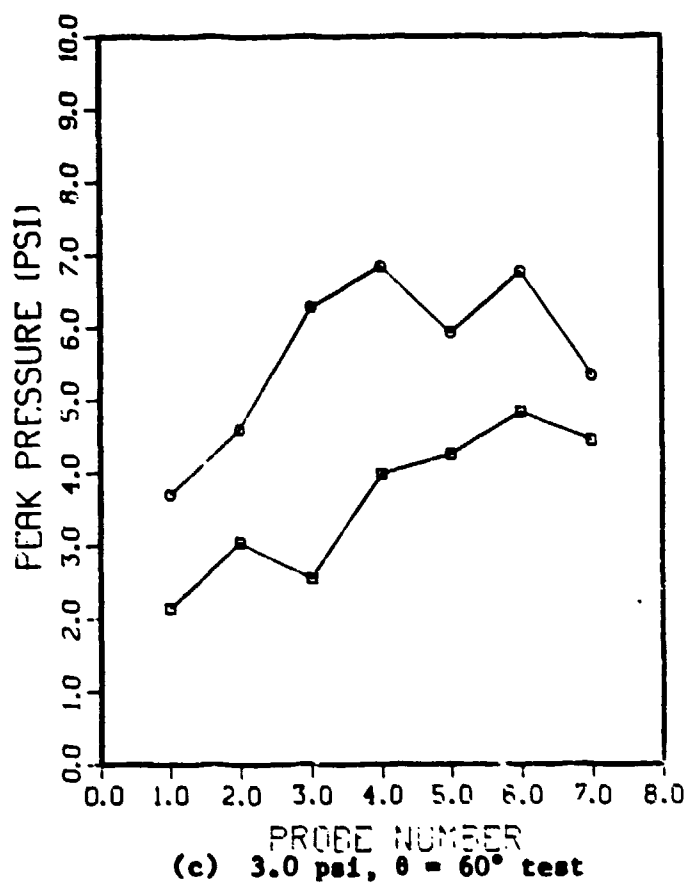
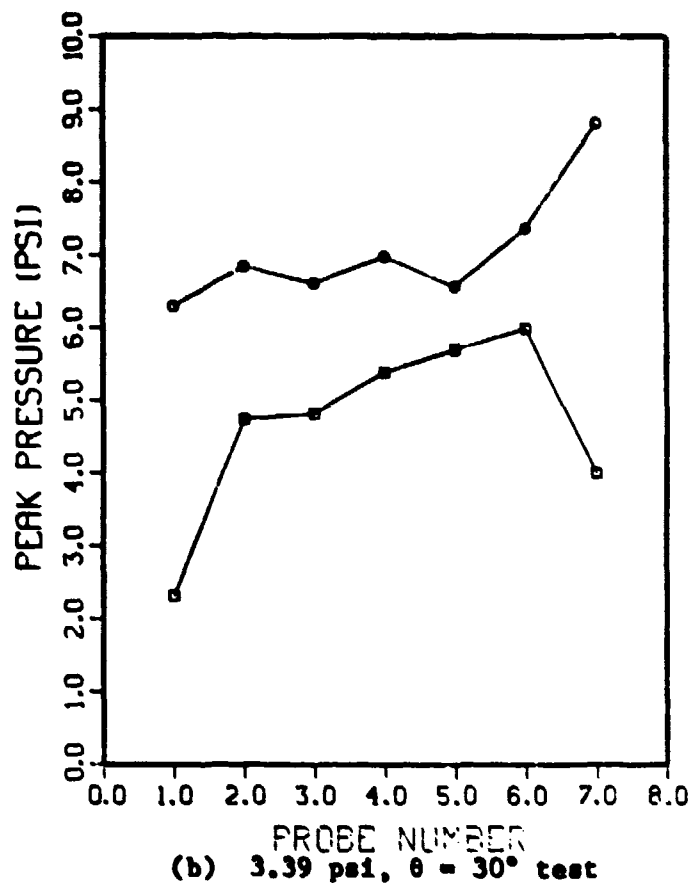
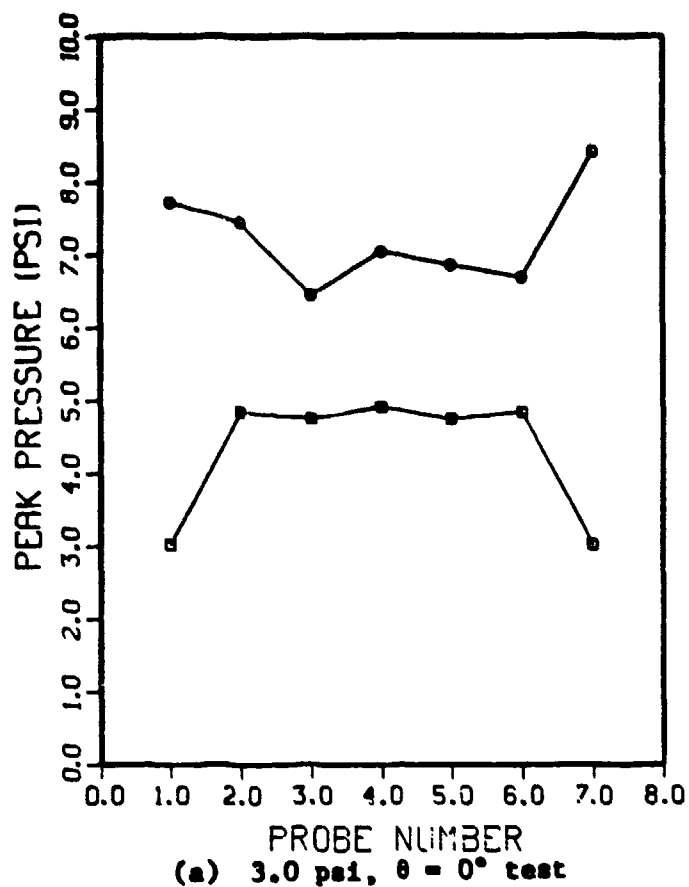
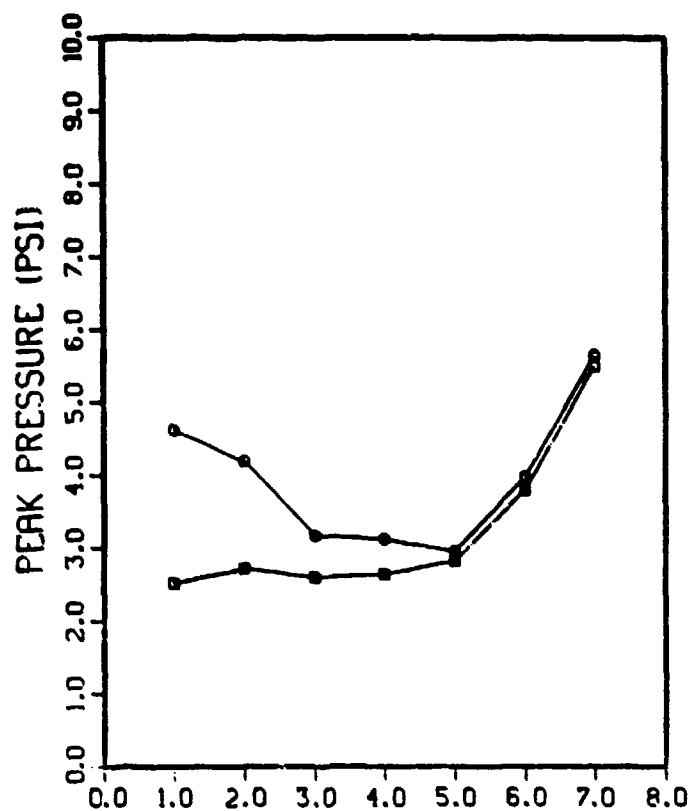
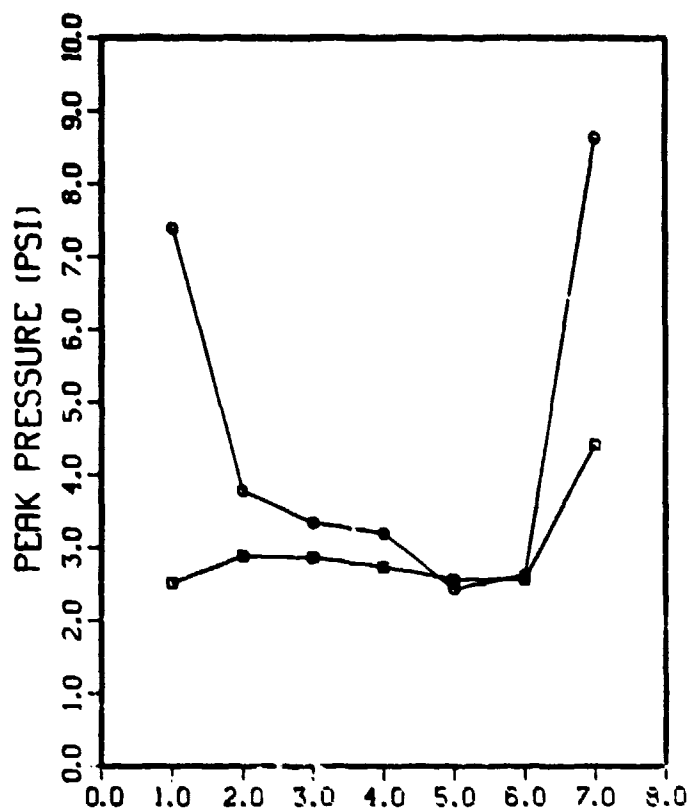


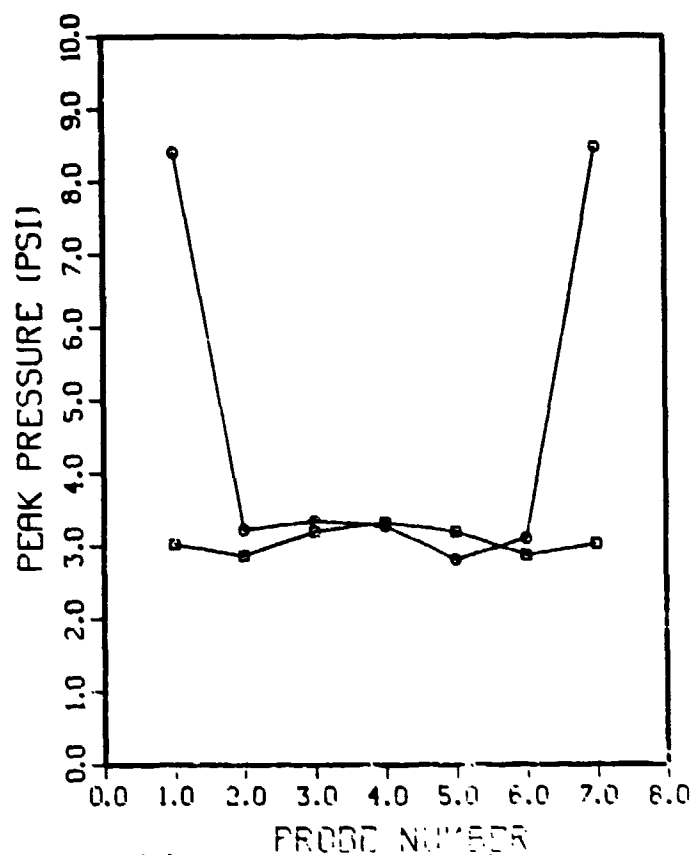
Figure 4-20. Comparison of calculated (\square) and measured (\circ) peak pressures.



(e) 3.61 psi, $\theta = 120^\circ$ test



(f) 3.69 psi, $\theta = 150^\circ$ test



(g) 3.84 psi, $\theta = 180^\circ$ test

Figure 4-20. (Cont'd).

Figure 4-20(a)-(g) shows comparisons of calculated and measured peak pressures at the various probe locations for all body orientations for the 3 psi experiments. The experimental peak pressures are consistently higher than those calculated, because of the smoothing influence of the finite resolution. Finer mesh sizes would be expected to capture more of the peak value.

Figures 4-21(a)-(g) present comparisons of calculated and measured impulses for the various body orientations. Only the positive part of impulse has been compared. In these calculations we have not scaled the calculated free field impulse to the measured value. However, the agreement between the unscaled calculated and measured impulses is probably within the experimental variation.

4.4 RELATION OF LOAD IMPULSE TO FREE-FIELD IMPULSE

This section compares calculated and measured impulse loadings for several blast waves. The impulses described below are normalized to the calculated or measured free field impulse in each case.

Figure 4-22 compares calculated probe impulses across the chest for all seven body orientations, from $\theta = 0^\circ$ to 180° , for the 3 psi tests described above. The impulses in each calculation are normalized by the free field impulse. When the chest is exposed directly ($\theta = 0^\circ$) the impulse of the loading is nearly equal to the impulse in the free field signal. As the body turns, there is a slight reduction in this ratio. Figure 4-23 shows the normalized impulses for the 3 psi wave as measured. The data is more scattered but is in the same band and has the same approximate trend.

In Figure 4-24, normalized impulses are shown for various peak waves all at 0° orientations. The 26.92 psi results are measured values, while the 9.62, 5.61, and 3.0 psi results are EITACC calculated data. These results imply that as the peak pressure of the free-field wave increases, the load impulse becomes greater than the free field impulse, perhaps twice as great at 25 psi. This increase in load may explain part of the increase seen in the isoimpulse studies.

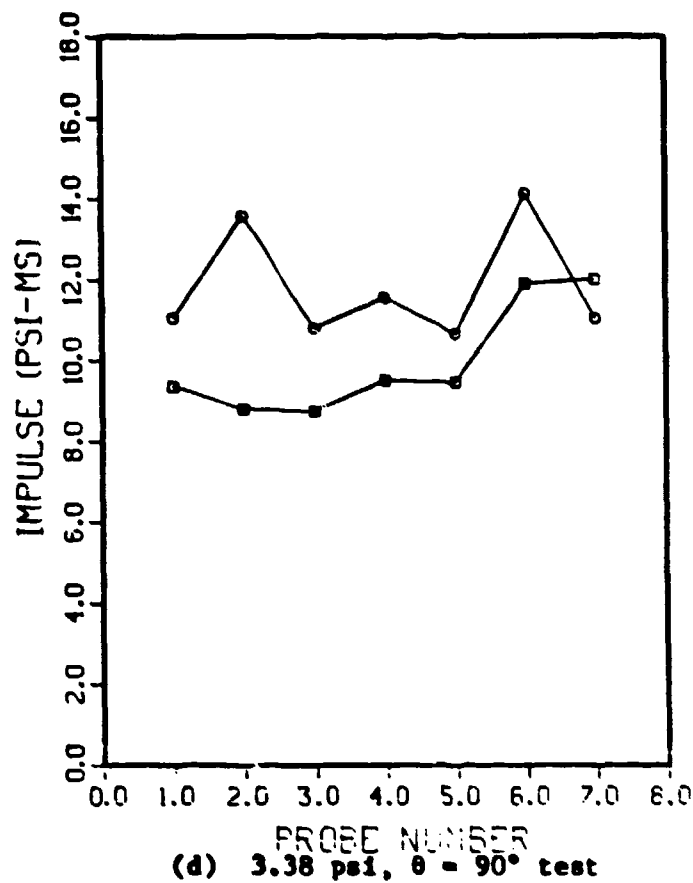
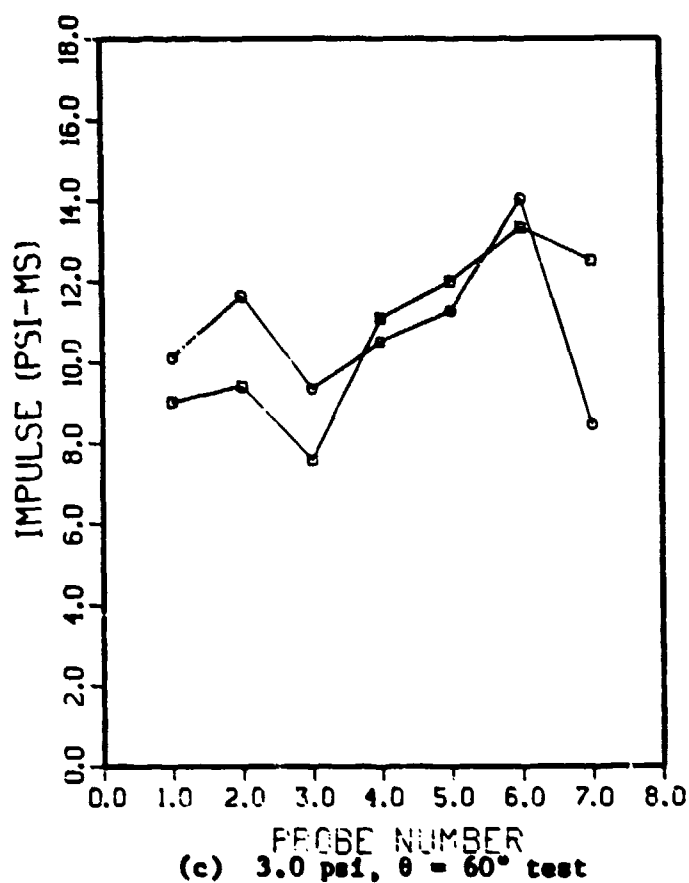
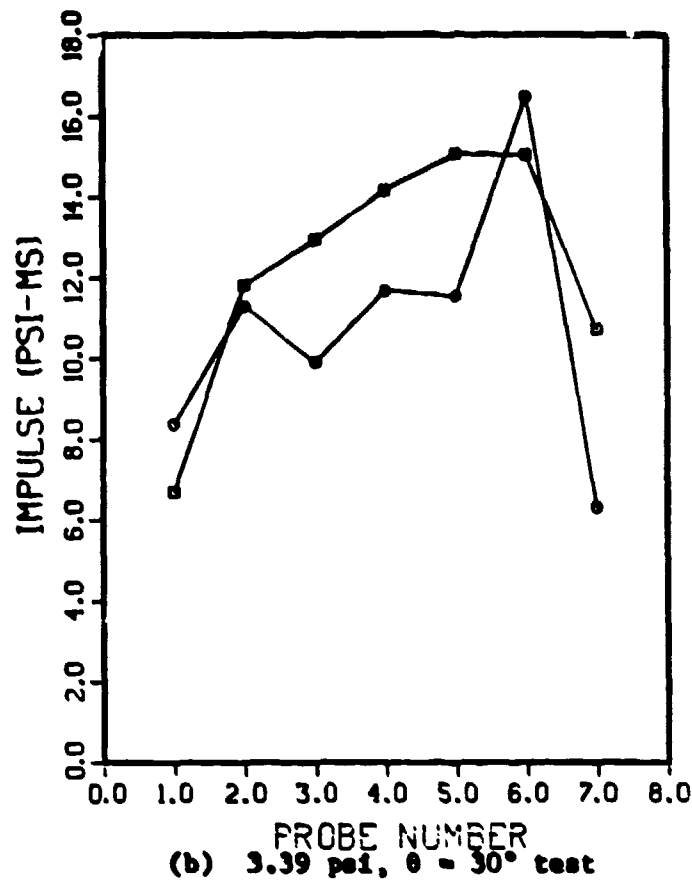
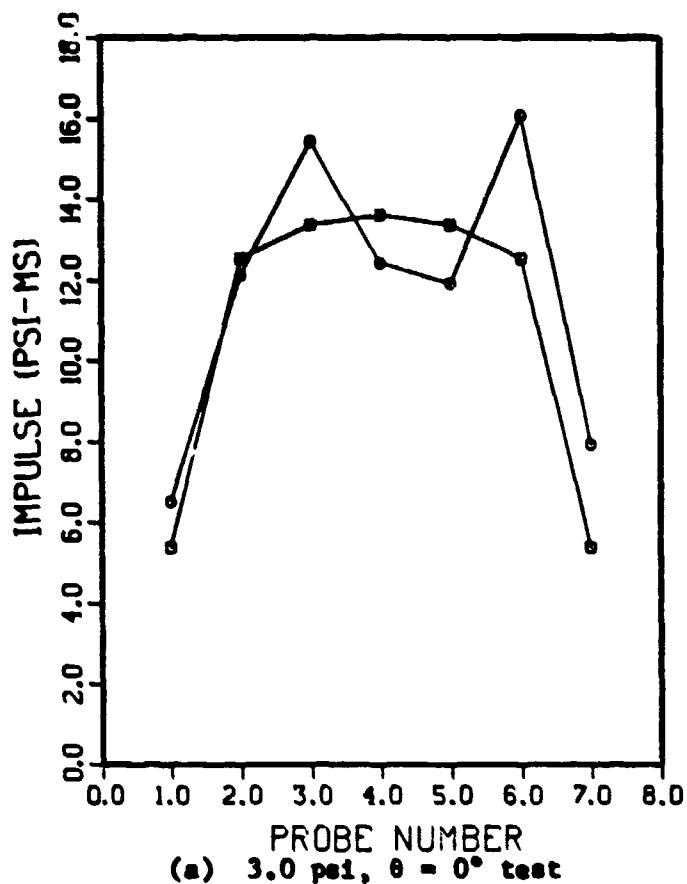
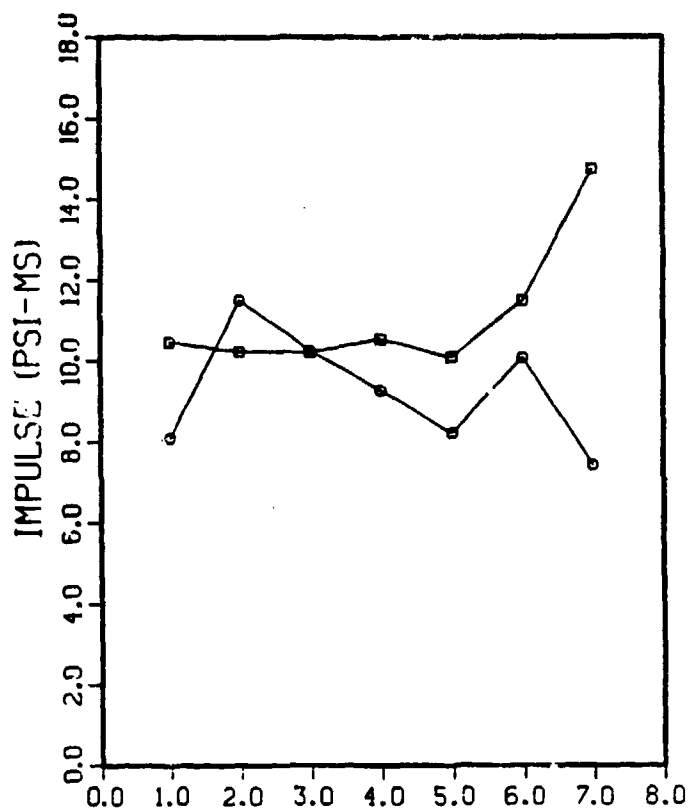
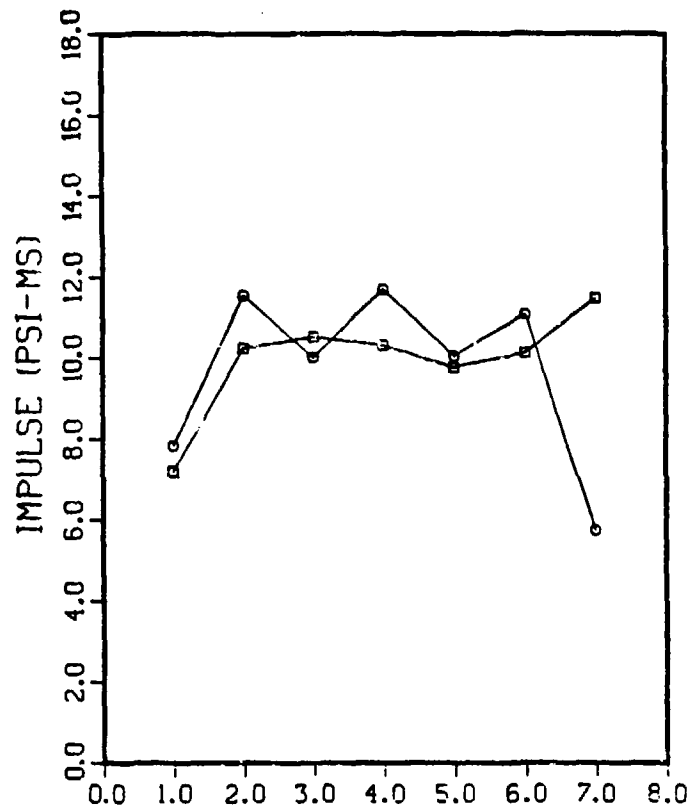


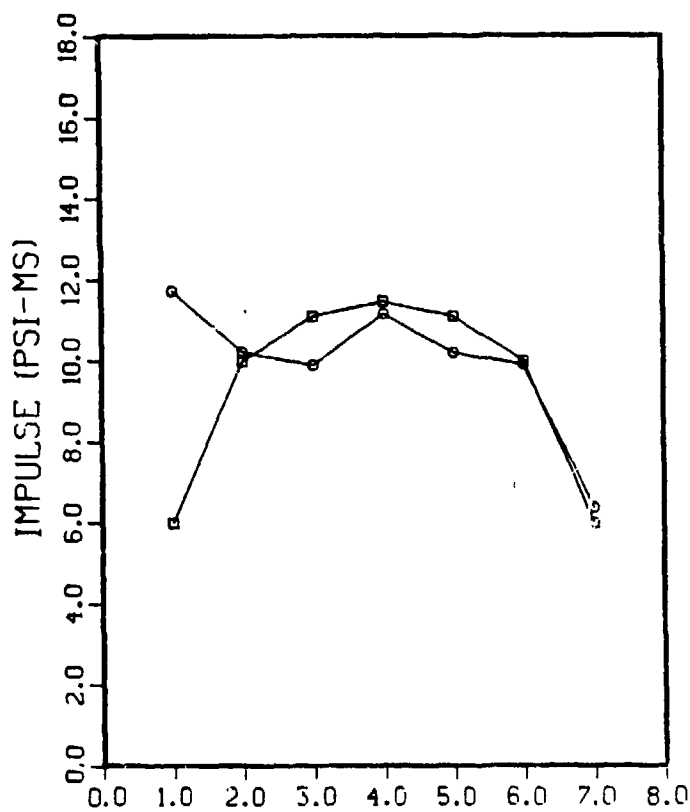
Figure 4-21. Comparison of calculated (\square) and measured (\circ) impulses.



(e) 3.61 psi, $\theta = 120^\circ$ test



(f) 3.69 psi, $\theta = 150^\circ$ test



(g) 3.84 psi, $\theta = 180^\circ$ test

Figure 4-21. (Cont'd).

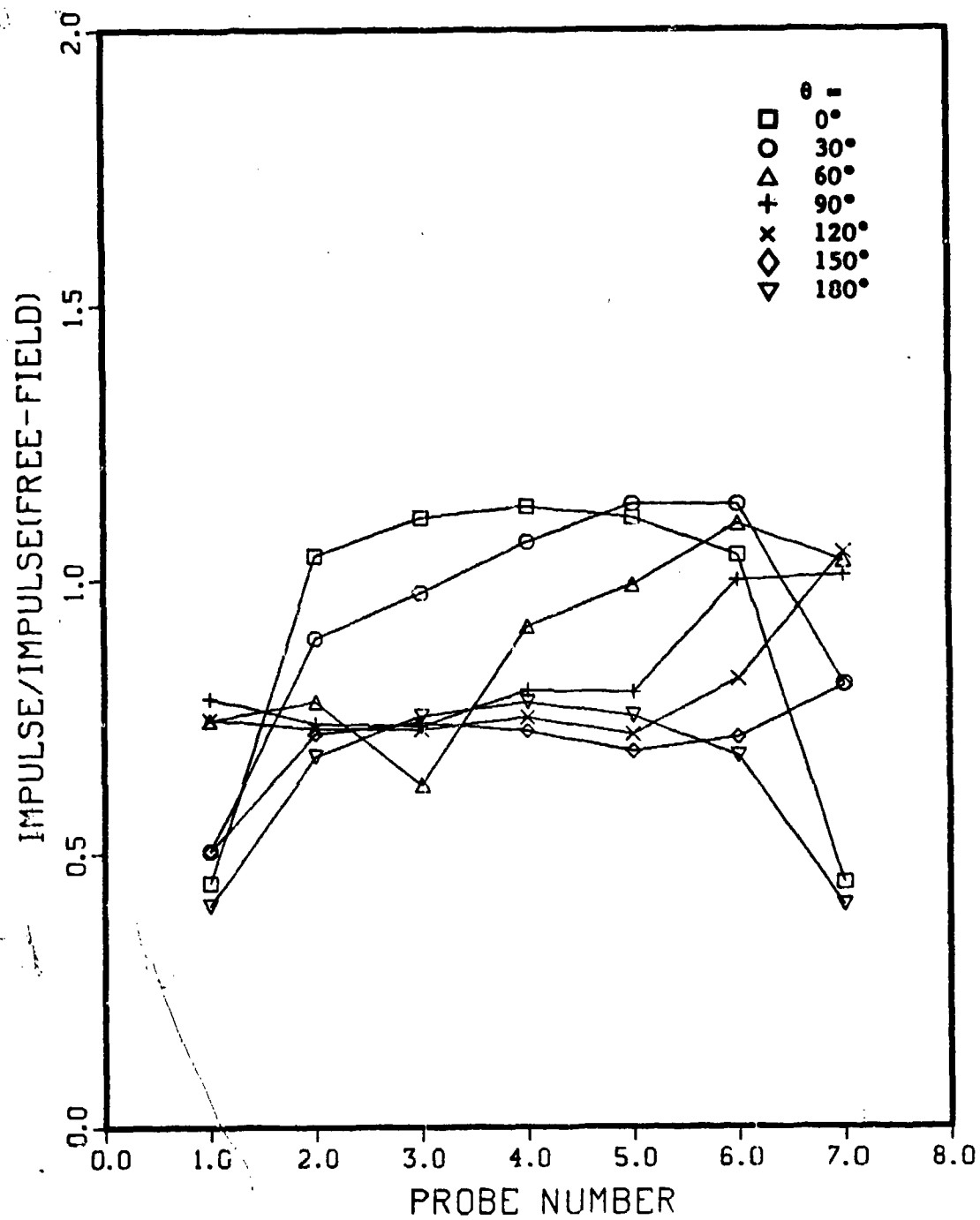


Figure 4-22. Comparison of calculated normalized impulsive loadings for nominal 3 psi tests

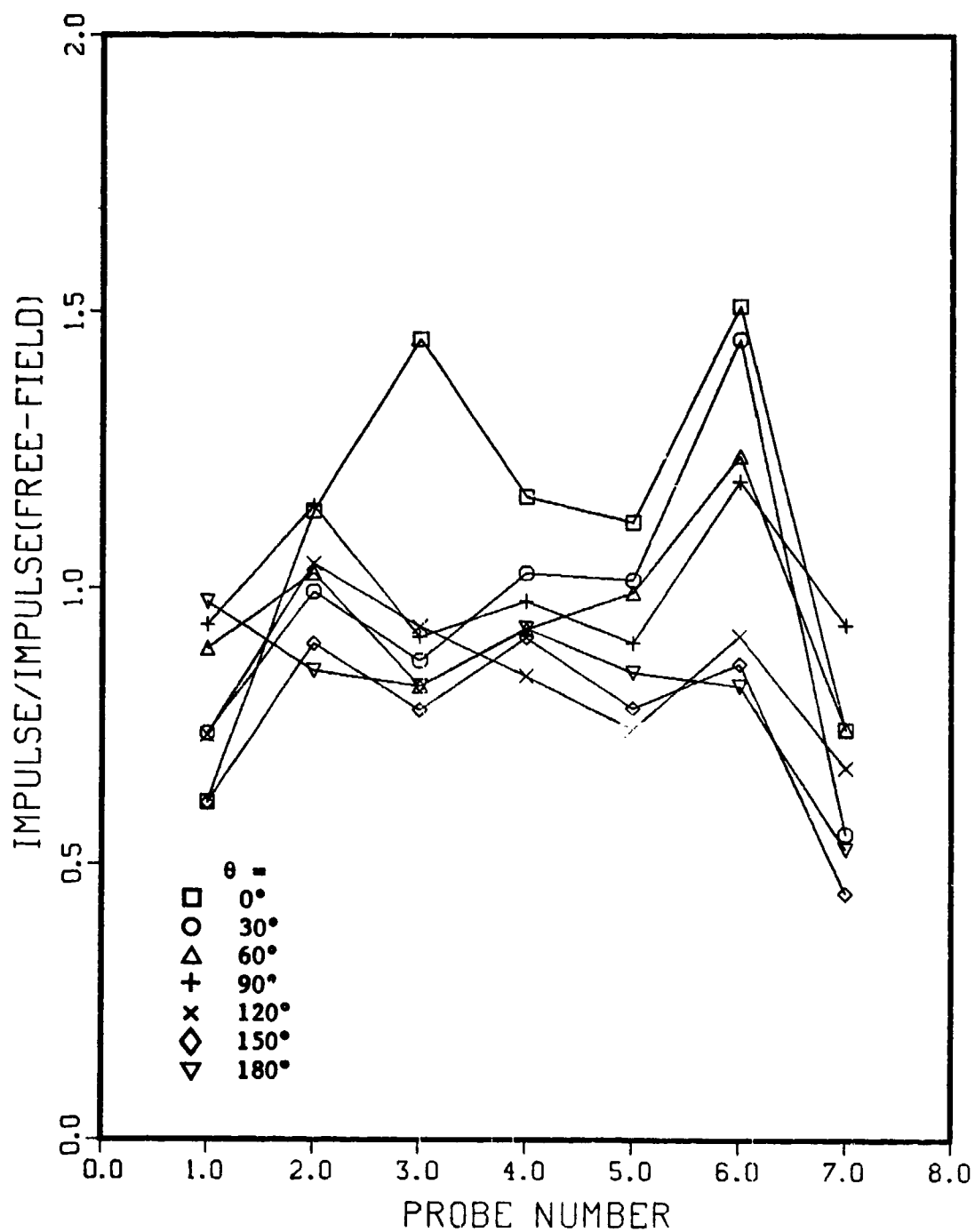


Figure 4-23. Comparison of measured normalized impulsive loadings for nominal 3 psi tests

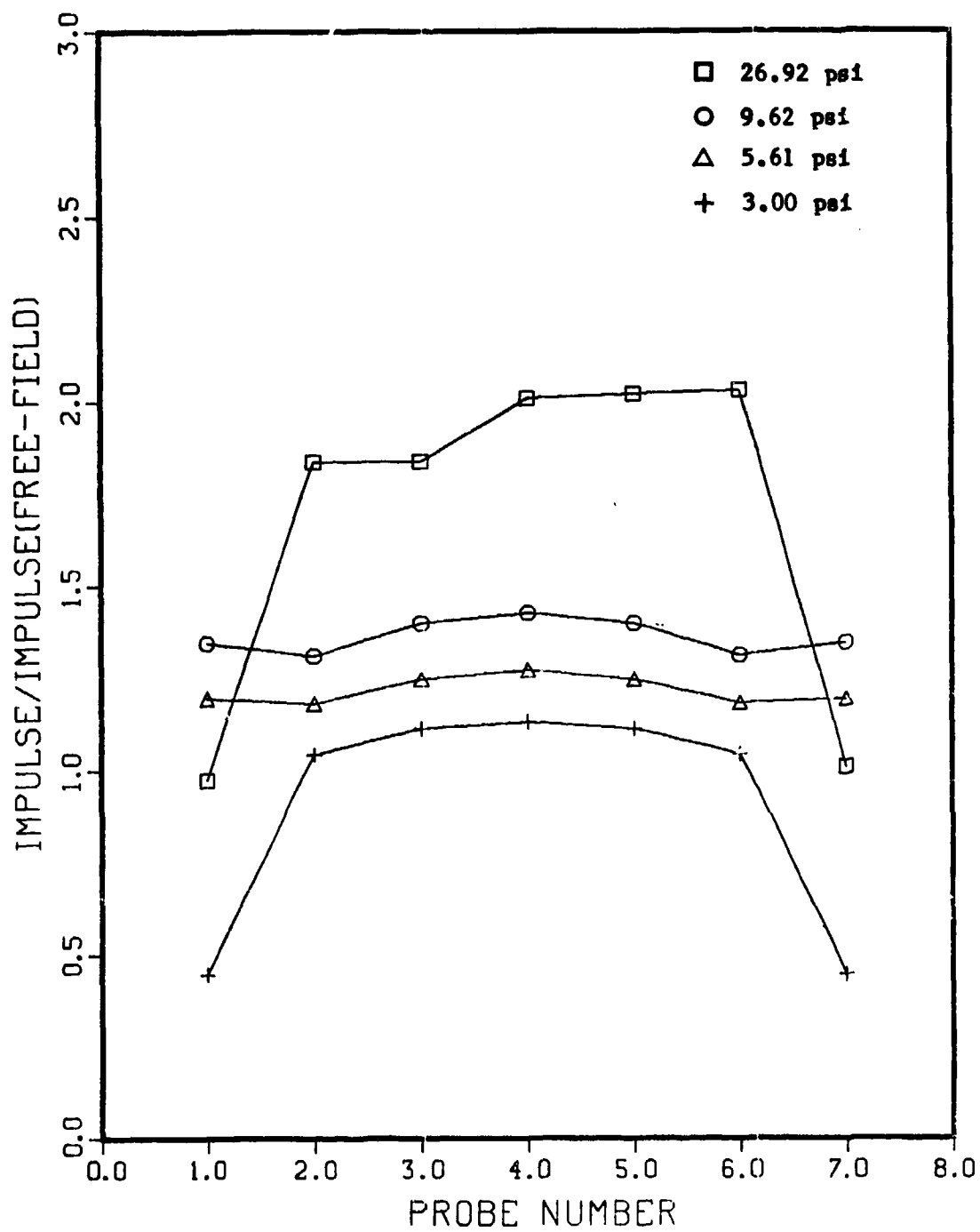


Figure 4-24. Comparison of higher pressure normalized impulse loadings for $\theta = 0^\circ$

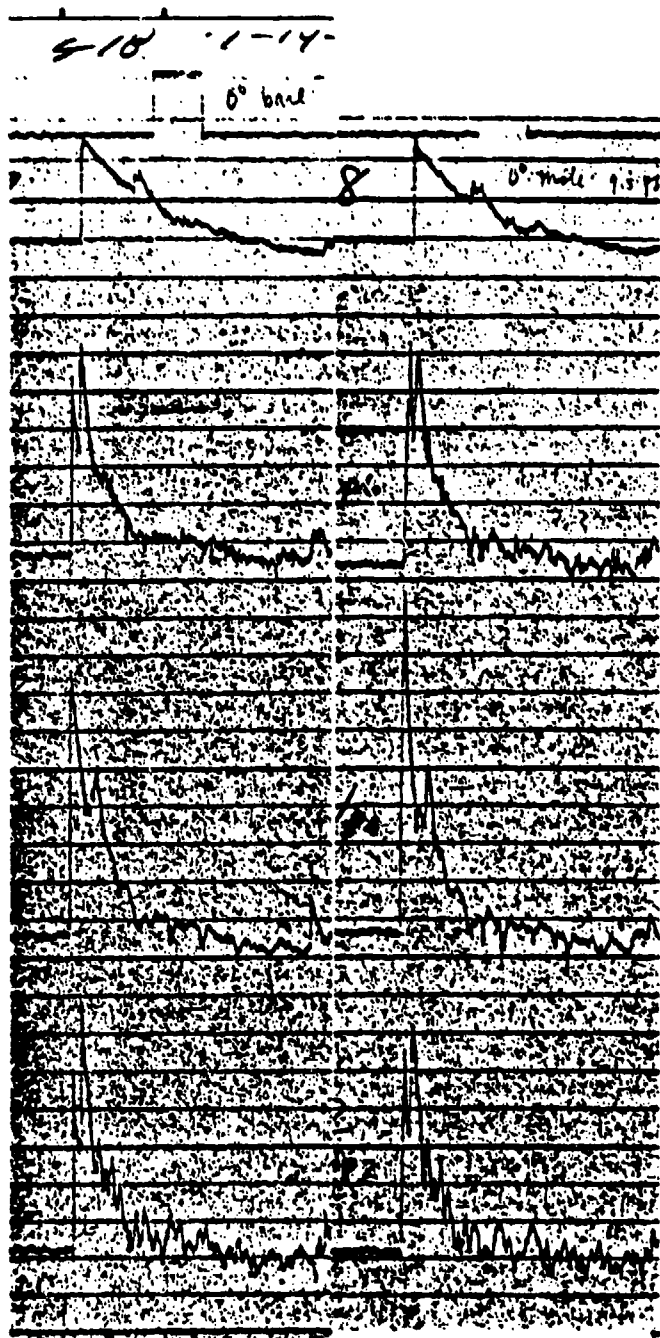
5. EFFECT OF SURFACE MATERIAL

Field experiments using human volunteers and anthropomorphic dummies indicate that clothing increases the measured intrathoracic pressure (ITP) by a statistically significant amount. Compliant surface material under a blast overpressure may lead to a higher internal response because of potential energy accumulated during the compression process redistributes the loading in time which provides better mechanical coupling to the body.

One of the objectives of the present task was to see whether variations in surface pressure could be traced to the material covering. The approach was to measure the pressure difference between the conditions when the model was covered with a compliant material and when it was not. For this purpose, runs were made at a nominal pressure of 9 psi for 0° and 90° orientations. For each case, the model was covered with a layer of foam-backed moleskin and tested under blast conditions identical to those without the covering.

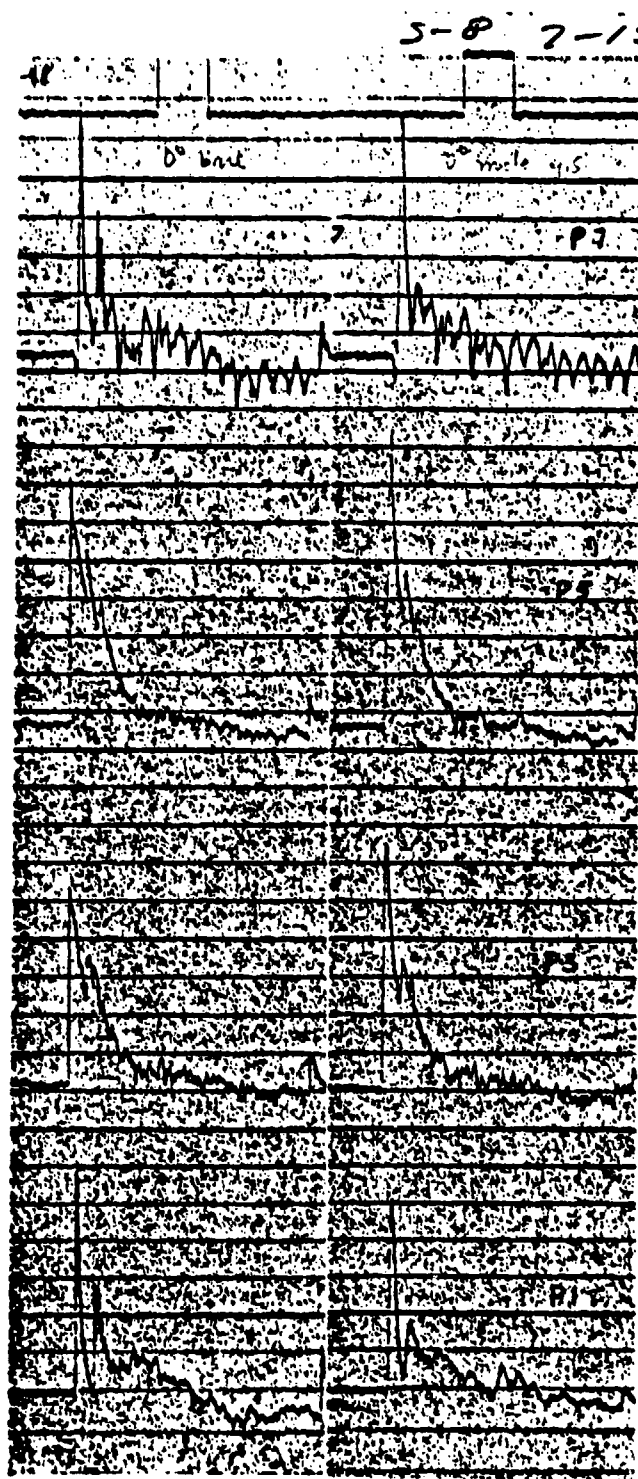
Figures 5-1 and 5-2 show the raw data of the two tests. For both cases, though they are similar in signal shape between the corresponding sets, there are differences in magnitudes. To facilitate comparison, both sets of data were non-dimensionalized by their respective reference pressures and replotted in Figures 5-3 and 5-4. An increase of 40% in peak pressure was produced for the 0° orientation at the center probe (where shock reflection occurs); at 90° (where there is little shock reflection) the effect is negligible.

A more systematic study of this phenomena is described in the report "Effects of Clothing on Thorax Response" (Volume 8 of this report).



a. Without cover
($P_o = 9.62$ psi)

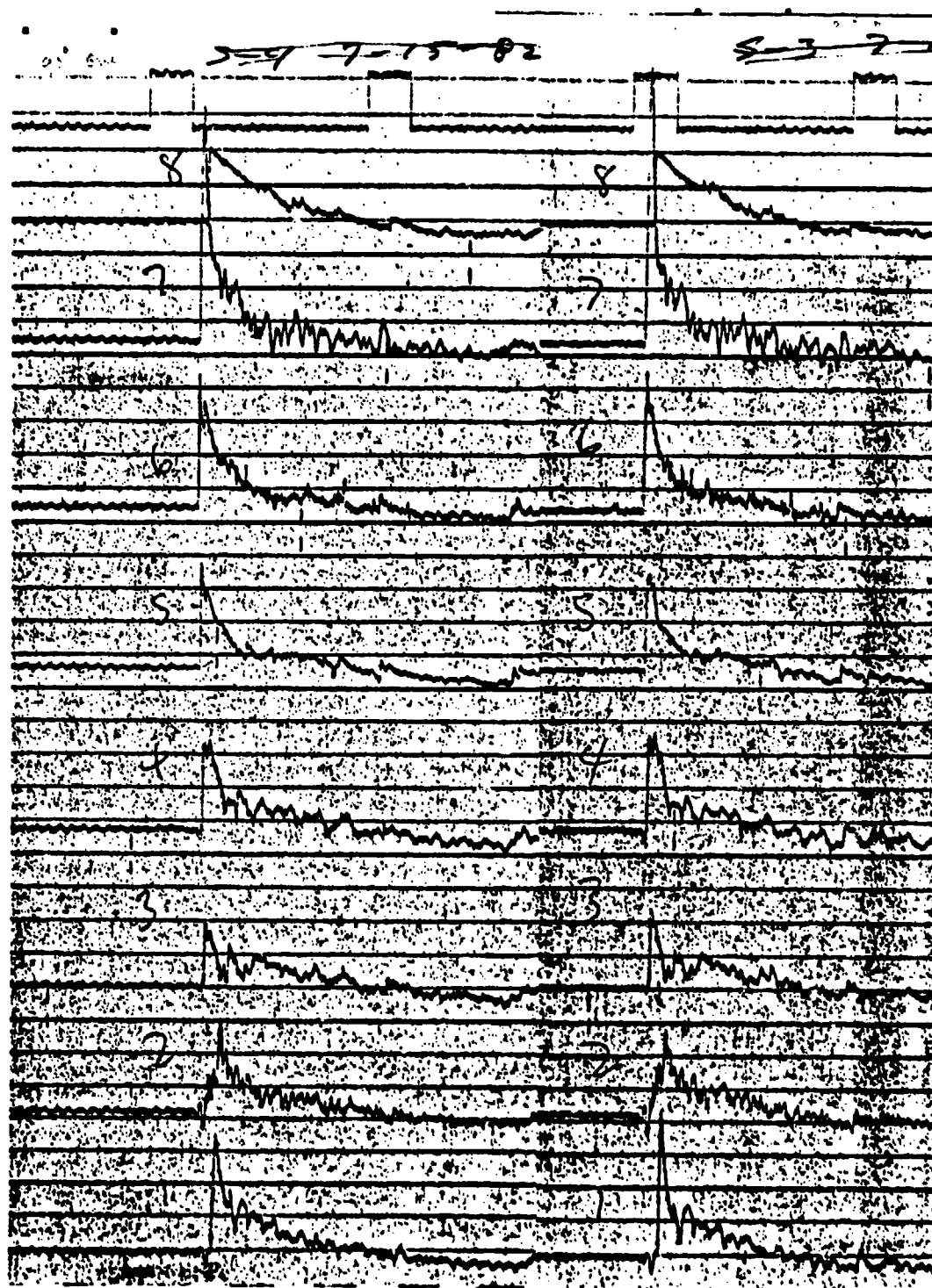
b. Covered with
Moleskin
($P_o = 9.42$ psi)



a. Without cover
($P_o = 9.62$ psi)

b. Covered with
Moleskin
($P_o = 9.42$ psi)

Figure 5-1. Effect of compliant surface on pressure signals at $\theta = 0^\circ$



a. Without cover
($P_o = 8.27$ psi)

b. Covered with moleskin
($P_o = 8.08$ psi)

Figure 5-2. Effect of compliant surface on pressure signals at $\theta = 90^\circ$

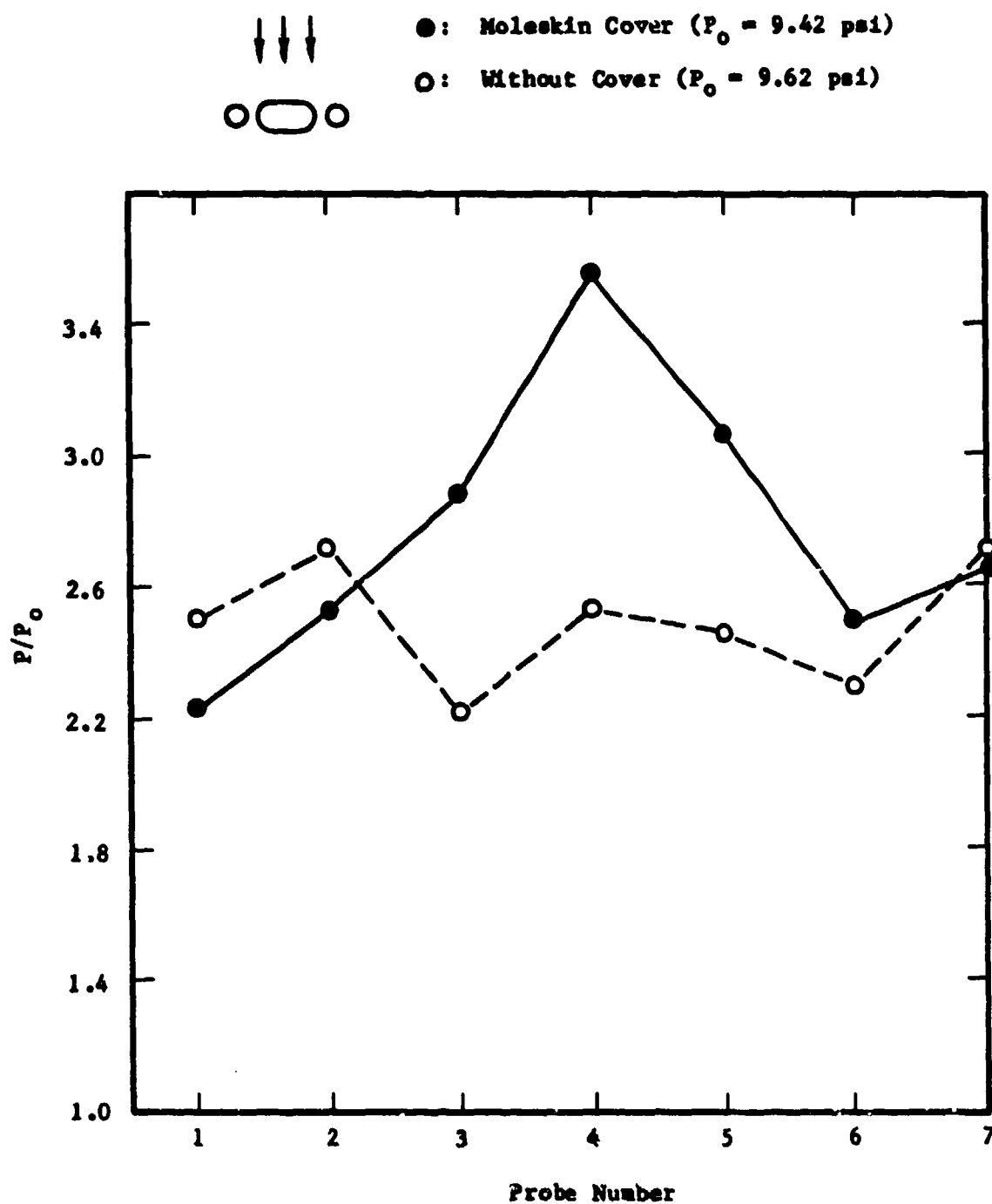


Figure 5-3. Effect of compliant surface on pressure distribution around a torso model at $\theta = 0^\circ$

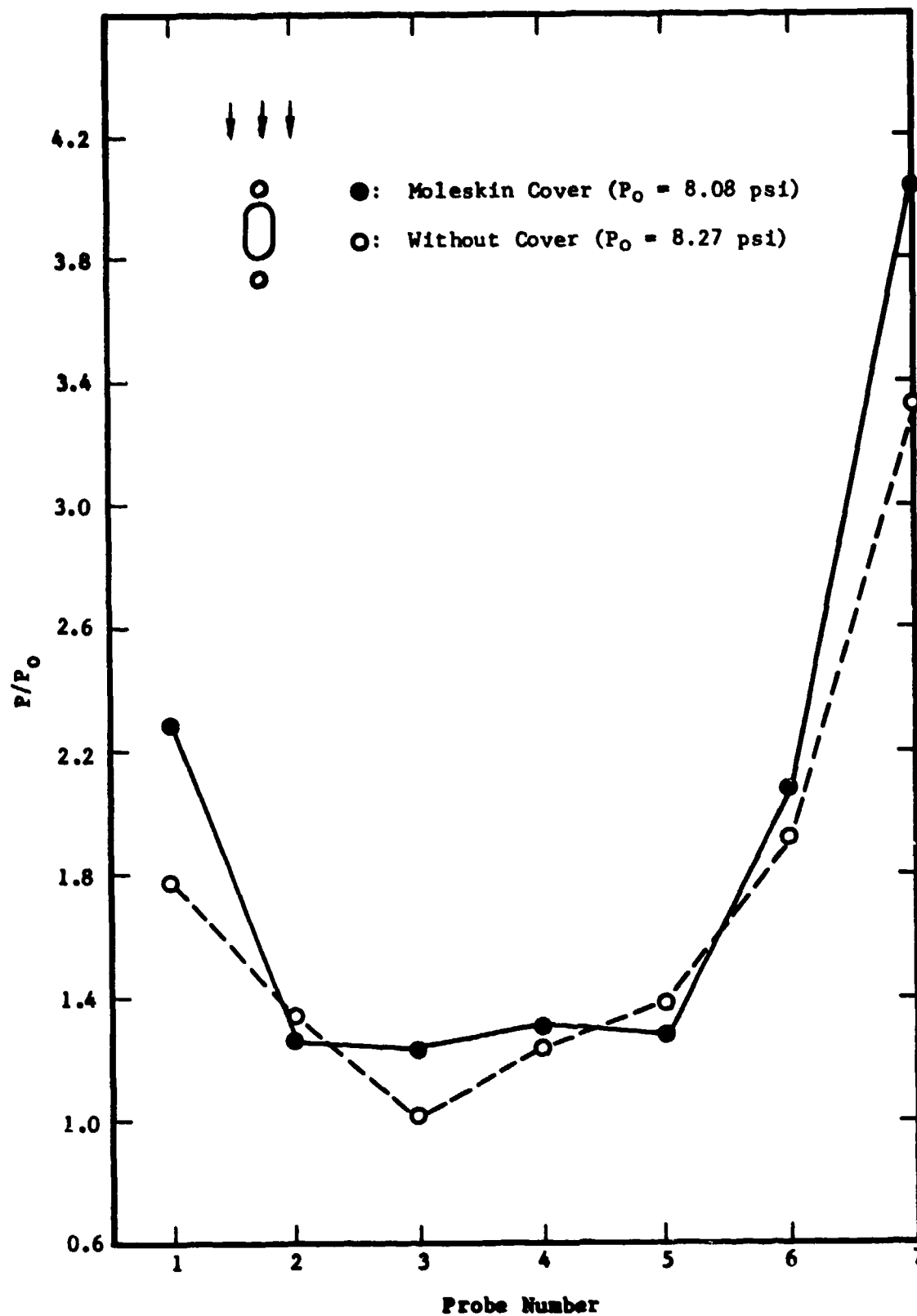


Figure 5-4. Effect of compliant surface on pressure distribution around a torso model at $\theta = 90^\circ$

6. SUMMARY AND CONCLUSIONS

The torso model designed and fabricated under this contract was able to satisfy the requirements for the field tests. Even at close proximity of the blast (slant range 16.9 ft), the model was able to withstand the heat stress and the intense pressure (up to 106 psi). The two copies are still available for further tests.

The field data acquired covered a wide range of parameters, and should be sufficient for present code validation purposes. Calibration factors varied by about 5% before and after the tests; shot-to-shot variations are unknown but are probably much larger.

The EITACC code is able to predict the shape and impulse of the pressure load distribution. Finer grids, smaller time steps, and a larger computation domain will be required to improve the prediction of the peak pressure value.

Possible pressure amplification at the model surface caused by the mole-skin cover suggests that more tests on the effect of clothing should be conducted.

DISTRIBUTION LIST

12 copies

**Director
Walter Reed Army Institute of Research
Walter Reed Army Medical Center
ATTN: SGRD-UWZ-C
Washington, DC 20307-5100**

1 copy

**Commander
US Army Medical Research and Development Command
ATTN: SGRD-RMI-S
Fort Detrick, Frederick, MD 21701-5012**

12 copies

**Defense Technical Information Center (DTIC)
ATTN: DTIC-DDAC
Cameron Station
Alexandria, VA 22304-6145**

1 copy

**Dean
School of Medicine
Uniformed Services University of the Health Sciences
4301 Jones Bridge Road
Bethesda, MD 20814-4799**

1 copy

**Commandant
Academy of Health Sciences, US Army
ATTN: AHS-CDM
Fort Sam Houston, TX 78234-6100**